学位論文

Heterogeneous Crustal Structure across a Seismic Block Boundary along the Nankai Trough off Cape Shionomisaki, Kii Peninsula: Application of Non-Linear P-wave Travel Time Inversion and Finite Difference Calculations to OBS Observation

潮岬沖南海トラフの地震ブロック境界における不均質地殻構造
— 海底地震計 データへの非線型P波速度インバージョン及び
有限差分法波形計算の応用 —

平成八年十二月 博士 (理学) 申請

東京大学大学院理学系研究科
地球惑星物理学専攻

望月 公廣

学位論文

Heterogeneous Crustal Structure across a Seismic Block Boundary along the Nankai Trough off Cape Shionomisaki, Kii Peninsula: Application of Non-Linear P-wave Travel Time Inversion and Finite Difference Calculations to OBS Observation

潮岬沖南海トラフの地震ブロック境界における不均質地殻構造
— 海底地震計 データへの非線型P波速度インバージョン及び
有限差分法波形計算の応用 —

平成八年十二月 博士 (理学) 申請

東京大学大学院理学系研究科
地球惑星物理学専攻

望月 公廣

Heterogeneous Crustal Structure across a Seismic Block Boundary along the Nankai Trough off Cape Shionomisaki, Kii Peninsula - Application of Non-Linear P-wave Tavel Time Inversion and Finite Difference Calculations to OBS Observation

by

Kimihiro Mochizuki

Earthquake Research Institute
University of Tokyo

Submitted in Partial Fulfilment
of the Requirements for the Degree of
Doctor of Science

December, 1996

Contents

List of Figures

List of Tables

Acknowledgment

I am grateful to Prof. Junzo Kasahara for his support and encouragements through my research at the Earthquake Research Institute, University of Tokyo. I am also grateful to the members of the laboratory, Mr. Sadayuki Koresawa, Dr. Toshinori Sato and Mr. Gou Fujie for valuable discussions and for their help in pursuing the research.

Thanks are due to Dr. T. Okamoto for providing me with his finite difference calculation codes and valuable advice on their development.

I greatly thank Dr. R. Hino, Dr. M. Shinohara and Mr. H. Nishisaka and other research members on the cruise of 1994 Nankai Trough experiment for their helps and advice.

I would like to thank Prof. N. Hirata, Prof. T. Iwasaki, Prof. T. Urabe, Prof. K. Koketsu, Dr. S. Sakai and other members of the seminar on structural heterogeneities for the valuable discussions and advice.

Mr. T. Hatori and Mr. N. Takeuchi gave me advice on waveform calculation according to their experience, which have been very helpful.

I also thank Prof. Y. Fukuda for providing me with the gravity data and helpful advice and comments.

I acknowledge stimulating discussions with Prof. Y. Fukao on shallow structure of the Nankai Trough.

I am indebted for critical reviews to the members of the dissertation committee: Prof. K. Suyehiro, Prof. T. Iwasaki, Prof. J. Kasahara, Prof. K. Shimazaki, and Prof. H. Tokuyama.

I thank all the staffs of Earthquake Prediction Research Center. Everything has been well organized, and always ready for use.

I owe wonderful school life at the institute to all of my good friends. I admire serious mentality of my best foreign friends: A.O, D.G, and D.L. Thanks very much to you all.

Abstract

The Nankai Trough, which runs along the outer coastline of south-western part of Japan and is formed as the Philippine Sea Plate subsides beneath the Eurasia Plate, is known for big earthquake generations in its history. Earthquakes have occurred rather systematically with fairly constant recurrence periods of 100 years for the earthquakes after the 1605 event and of 200 years for those prior to the event. According to the latest studies on the most recent earthquakes of the Tonankai (1944) and the Nankaido (1946) earthquakes, the fault zone along the Nankai Trough are composed of four mutually mechanically decoupled rupture zones. The most prominent seismic boundary of these rupture zones runs south to the Cape Shionomisaki at the tip of the Kii Peninsula.

A seismic refraction-reflection experiment was conducted in 1994 at the supposed location of the seismic boundary off the Kii Peninsula. The main object of the experiment is to ascertain whether a positive relationship exists between earthquake activities and structural heterogeneity.

A two-dimensional P-wave travel time non-linear inversion scheme was developed in this study, and it was applied to the above experiment. The crust of the subducting Philippine Sea Plate changes its thickness beneath the Shionomisaki Canyon where the seismic boundary is supposed to run, and the eastern crust is thicker. This change of the thickness is also confirmed on the gravity data, as the two-dimensional synthetic gravity anomaly calculated with respect to the velocity structure obtained by the travel-time inversion matches the

observed gravity. The location of the change of the gravity anomaly from negative to positive values corresponds to the location of the Shionomisaki Canyon.

As it gets common that an ocean bottom seismometer (OBS) is equipped with an A/D converter so that digital recording becomes possible, more accurate discussion can be made on observed waveforms. A synthetic waveform calculation method utilizing the fourth-order finite difference operator for seismic experiments in the ocean is developed and also applied to the 1994 Nankai Trough experiment. The calculated waveforms with respect to the resultant model of the travel-time inversion are compared with the observed waveforms. A good match is seen, and the validity of the structure model is confirmed.

Chapter 1

GENERAL INTRODUCTION

1.1 Tectonic Settings

The Japanese islands are an assembly of the tectonic segments which belong to the four different plates, and the plate boundaries run through and around the islands (Seno & Sakurai, 1996). Those plates are the Eurasia Plate, the Philippine Sea Plate, the Pacific Plate and the Okhotsk Plate, in the counterclockwise order from the northwest (Figure 1.1). The Eurasia Plate includes the Japan Sea, the western half of the main island and the other southwestern islands. The Philippine Sea Plate holds the Izu Peninsula and the other southern islands. The northeastern part of the main island and the northern islands sit on the Okhotsk Plate. The Pacific Plate forms the prominent geographic structures of the Japan Trench and the Izu-Bonin Trench, as it subsides beneath the Okhotsk Plate and the Philippine Sea Plate, respectively. This geographic configuration complicates the stress field over the Japanese islands and various types of earthquake generations are the manifestation of this complexity.

The Nankai Trough, the eastern part of which is the target area of this study, is

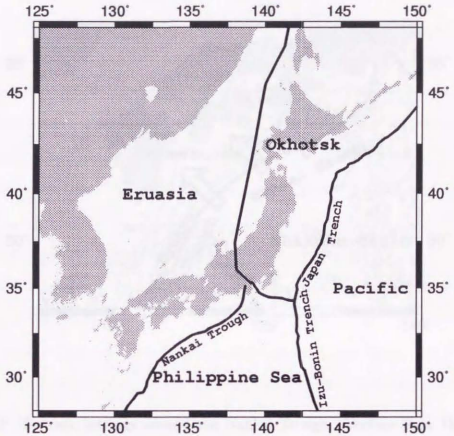

Figure 1.1: Plate geometry around Japan (Seno & Sakurai, 1996).

formed between the Eurasia and the Philippine Sea Plates, as the Philippine Sea Plate subsides beneath the Eurasia Plate at the rate of about 43 mm/yr (Seno, Stein & Gripp, 1993). The trough spans 700 km with the NE-SW orientation, having the eastern end at the base of the Izu Peninsula in the Suruga Bay and the other end off the southeast Kyushu island where the Kyushu-Palau Ridge on the Philippine Sea

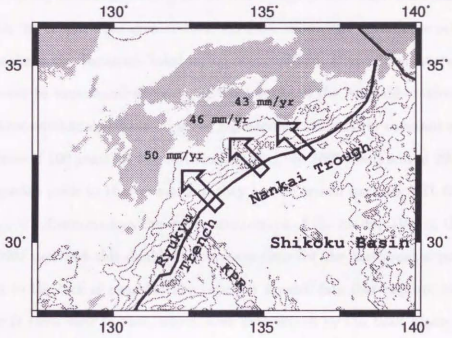

Figure 1.2: Tectonic settings around the Nankai Trough. Vectors show the relative velocities of the Philippine Sea Plate with respect to the Eurasia Plate (after Seno et al. (1993)). The location of the Kyushu-Palau Ridge is indicated by KPR.

Plate subsides beneath the Eurasia Plate (Figure 1.2). The trough is joined to the Ryukyu Trench at the western end. The Nankai Trough is relatively shallow, reaches only 4900 meters deep and is filled with the sediment which consists of the turbidite in the upper half and the hemipelagic mudstone in the lower half. The trough is known for its big earthquake generations in the history.

1.2 Seismic Activity

The historical big earthquakes along the Nankai Trough in the Tokai-Tonankai-Nankaido region with the magnitudes greater than 7.0 have shown the systematic occurrences: an earthquake in the Tonankai-Tokai region occurred and, after a time interval ranging from a second to some hundred years, an earthquake in the Nankaido region followed. Pairs of these earthquakes have occurred repeatedly with a fairly constant seismic recurrence time of 100 years for the earthquakes after the 1605 event and of 200 years for the earthquakes prior to that event, and they can be traced back to A.D. 684 (Ando, 1975). Figure 1.3 summarizes the cyclic occurrences of the earthquakes in this region. Scholz (1990) ascribed this doubled recurrence time for the earthquakes prior to the 1605 event to the lack of records. The region is divided into four rupture zones, Zone A to Zone D from west to east, which were determined by the fault plane studies of the 1944 Tonankai and the 1946 Nankaido earthquakes. This distribution of the rupture zones explains well the geodetic observations and other physical evidence such as the damages caused by the tsunamis for the most recent five earthquakes occurring in this region, including the two above-mentioned earthquakes. These four rupture zones are thought to be mechanically decoupled from one another, with the most distinctive decouple being between Zone B and Zone C. In Figure 1.3, the rupture lengths which slipped in each event are also indicated. The source mechanisms of these earthquakes are similar and are interpreted as the low-angle reverse faulting with the oceanic plate underthrusting north-westwards against the continental plate (Ando, 1975).

Among the earthquakes in this region, there have been intensive studies of the most recent 1944 Tonankai and 1946 Nankaido earthquakes (Fitch & Scholz, 1971; Kanamori, 1972; Ando, 1975; Ando, 1982; Kato, 1983). These studies suggest that the seismic

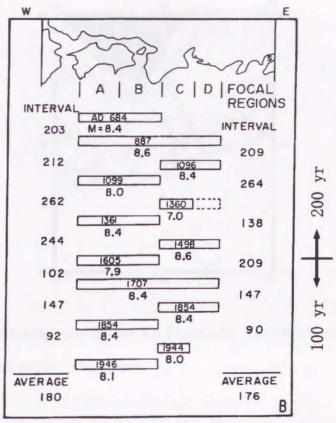

Figure 1.3: History of earthquakes along the Nankai Trough. The region is divided into four rupture zones. The boxes indicate rupture lengths and dates of earthquakes. The intervals between earthquakes are also indicated. Average recurrence periods are 100 years for the earthquakes after the 1605 event, and 200 years for those prior to that event. (Scholz, 1990)

fault plane boundary between these two neighboring earthquakes runs southeast from the southern tip of the Kii Peninsula (the boundary between Zone B and Zone C in Figure 1.3), where the distinctive topographic structure of the Shionomisaki Canyon runs perpendicular to the trough axis (Figure 1.4). Figure 1.5 shows that the

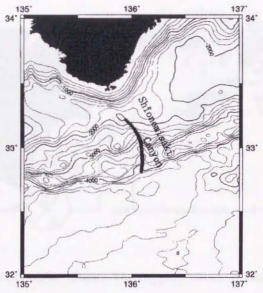

Figure 1.4: Seafloor topography off the Kii Peninsula. The Shionomisaki Canyon runs almost perpendicular to the trough axis.

epicenters of both earthquakes were determined in the vicinity of this seismic boundary, and Figure 1.6 shows that their aftershock distributions are separated by the boundary (Kanamori, 1972). The determined fault slip length differs among the fault models by only slightly, and their average is calculated to be four meters for both earthquakes, which is consistent with the 100 year recurrence period considering that the Philippine Sea Plate subsides at the rate of about 43 mm/yr. The fault plane boundary between Zone B and Zone C can also be seen on today's seismicity map (Figure 1.7).

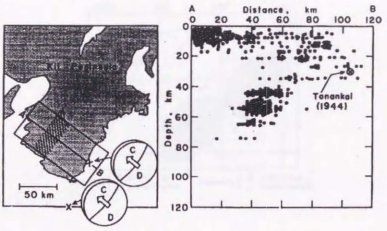

Figure 1.5: Figure on the right shows the hypocenters of small earthquakes in the rectangular region shown in the figure on the left during the period from January to July, 1969. Hypocenters are projected on the vertical plane along AB on the left figure. The mechanism diagrams and the slip vectors of the Tonankai and the Nankaido earthquakes are shown in the figure on the left. (Kanamori, 1972)

1.3 Overriding Plate: Kii Peninsula

The velocity structure beneath the Kii Peninsula has been studied by several authors (Mizoue, 1971; Mizoue, Nakamura, Seto & Ishiketa, 1983; Hori, Inoue, Fukao & Ukawa, 1985).

Hori et al. (1985) studied the origin of the prominent later phases observed after both P- and S-first arrivals. They constructed a two-dimensional velocity structure model along the lines running almost parallel to the trough axis across the peninsula so that the structure model explains the travel times of the P- and S-first arrivals and of their later phases (Figure 1.8).

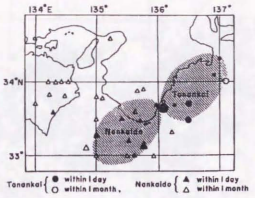

Figure 1.6: Aftershock distributions of the Tonankai (circle) and the Nankaido (triangle) earthquakes. Filled circles and triangles are aftershocks within one day and open circles and triangles are those within one month after the main shocks. Dimensions of circles and triangles correspond roughly to the magnitude of earthquakes. The hatched zone shows the assumed fault surfaces. (Kanamori, 1972)

The upper boundary of the subcrustal seismic activity has been known to be extensively concave beneath the Kii Channel (Mizoue et al., 1983), and Hori et al. (1985) revealed the excessively hollow structure of the subducting Philippine Sea Plate (Figure 1.8). The steepest fall line of the upper boundary of the subcrustal seismic activity runs perpendicular to the Nankai Trough, and its extension may meet the Shionomisaki Canyon (Figure 1.8). According to Mizoue et al. (1983), the activity of microearthquakes beneath the Kii Peninsula constructs a three layering structure (Figure 1.9). From the top to the bottom, they are 1) the shallow uppercrustal activity (focal depth < 15 km), 2) the transitional activity near the Mohorovičić discontinuity ($15 \leq$ f.d. ≤ 35) and 3) the subcrustal activity ($35 \leq$ f.d.). The focal mechanism distribution in the layers are the E-W compression reverse fault for the uppercrustal activity

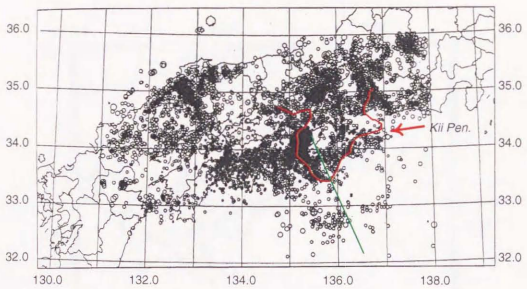

Figure 1.7: Recent seismic activity in western Japan from January, 1985, through December, 1992. Hypocenters were determined at Wakayama Micro-earthquake Observatory, Earthquake Research Institute, University of Tokyo. Green line indicates the location of the expected seismic boundary. The microseismic activity is more intense in the region west to the boundary.

and the NW-SE compression strike slip or the NW-SE extension normal fault for the subcrustal activity. The focal mechanisms of the transitional activity are divided into two groups and they are similar to the uppercrustal earthquakes in the upper-half and to the subcrustal earthquakes in the lower half of the layer. The complex distribution of the focal mechanisms suggests the complicated stress field which is determined by the force balance of the three mutually conflicting plates, i.e., the Eurasia, the Pacific and the Philippine Sea Plates. It is also worth noting that the microearthquake activity is intense beneath the western half of the Kii Peninsula and that it seems truncated

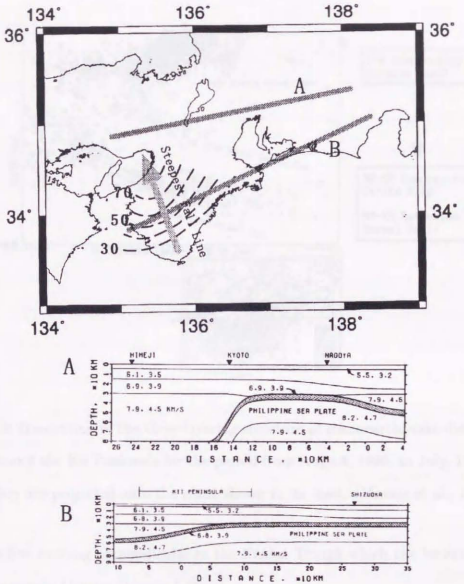

Figure 1.8: Velocity structure model beneath the Kii Peninsula along the lines, A and B, shown in the figure on the top. The contour in the figure on the top indicates the observed upper boundary of the subcrustal seismic activity. The vector of the steepest fall line is also shown. Numbers in each layer of the structure models indicate V_p and V_s (km/sec). The oceanic crust is indicated by stippling. (Hori et al., 1985)

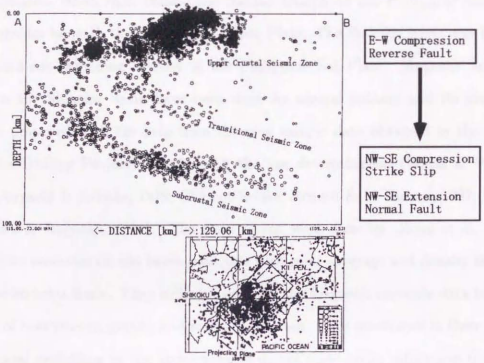

Figure 1.9: Illustration of the three-layering structure of microearthquake distribution in and around the Kii Peninsula for the period from August, 1980, to July, 1982. The hypocenters are projected onto the plane shown in its inset. (Mizoue et al., 1983)

along the line running perpendicular to the Nankai Trough which can be extended to the Shionomisaki Canyon (Figure 1.7).

1.4 Subducting Plate: Shikoku Basin

Since Occurrences of underthrusting earthquakes are driven by the frictional contact of a subducting and an overriding plates, the morphology and the physical properties

of a subducting plate should play an important role on earthquake generation. There lies the Shikoku Basin right behind the Nankai Trough on the Philippine Sea Plate and it subsides beneath the overriding Eurasia Plate. The Shikoku Basin was formed by the back-arc spreading activity in the Philippine Sea Plate. Magnetic anomaly studies in the Shikoku Basin have been done by several authors and its evolution has been proposed with the help from the core sample data obtained in the DSDP (Deep Sea Drilling Project) Leg 58 with the age determination (Watts & Weissel, 1975; Kobayashi & Nakada, 1978; Chamot-Rooke, Renard & Le Pichon, 1987; Okino, Shimakawa & Nagaoka, 1994). The most recent work done by Okino et al. (1994) proposed its evolution on the latest data sets with good coverage and density through the entire Shikoku Basin. They collected not only the magnetic anomaly data but also the data of bathymetry, gravity and seismic reflection. As is mentioned in their paper, the proposed evolutions by the above authors do not show major differences from one another. However more data were collected and the resolution was highly improved so that it became possible to discuss its evolution in detail with more confidence. The proposed evolution will be introduced briefly in the following, based mainly on Okino et al. (1994).

The evolution of the Shikoku Basin consists of five stages (Figure 1.10). 1) The rifting activity started before 30 Ma at the eastern flank of the Kyushu-Palau Ridge and the rifting sequence throughout the basin was completed near 26 Ma (Figure 1.10-A). 2) The opening stage started at 26 Ma in the northern part of the basin and propagated southward at the speed of 10 cm/yr. The opening was symmetric along the axis with the half spreading rate of 4.5 cm/yr and the axis had the NNW-SSE orientation (Figure 1.10-B). 3) The opening axis rotated clockwise near 23 Ma with the new orientation of

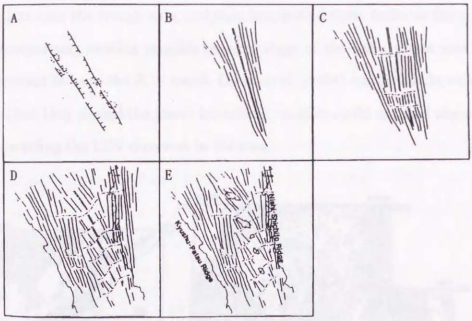

Figure 1.10: Evolution of the Shikoku Basin. See text for explanation. (Okino et al., 1994)

the N-S trend. Three transform faults were made due to the adjustment of the opening axis to the new orientation accompanied by axis segmentations. The spreading rate was abruptly decreased to 2.2 cm/yr, about the half of the previous rate, at 22 Ma (Figure 1.10-C). 4)The spreading axis rotated counterclockwise with the new orientation of the NW-SE trend at 19 Ma. The rotation sequence was slowly accomplished in the southern part to 31.5 N, resulting in the curved transform faults and the fan shaped seafloor (Figure 1.10-D). 5) The opening process ceased at 15 Ma, which was synchronized with the opening of the Japan Sea. The Kinan Seamount Chain was formed on the axis grabens. The northern part of the basin has been deformed, which can be the result from the backarc opening of the Japan Sea (Figure 1.10-E).

Chamot-Rooke et al. (1987) found three faults trending the N-S direction on the subducting plate near the trough axis, and they interpreted these faults as the transform faults accompanying another possible opening stage of the basin whose axis orientation is expected to be of the E-W trend. Okino et al. (1994) confirmed the existence of the faults, but they denied the above hypothesis, as they could not find any magnetic anomaly trending the E-W direction in the area.

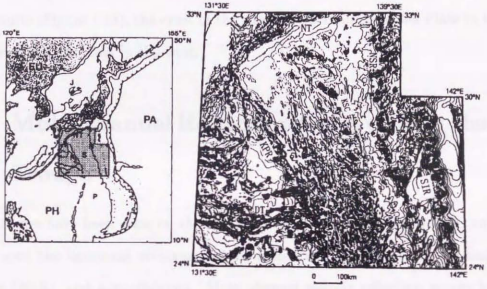

Figure 1.11: Topography of the Shikoku Basin obtained by SEABEAM survey. The survey region is indicated by stippling in the figure on the left. Contour interval is 200 m. (SIR: Shichito-Iwojima Ridge. NSR: Nishi-Shichito Ridge. KSC: Kinan Seamount Chain. NT: Nankai Trough. KPR: Kyushu-Palau Ridge. DT: Daito Ridge.) (Okino et al., 1994)

The topographic features of the Shikoku Basin retain the spreading axis orientation of the NNW-SSE trend (Figure 1.11), which suggests that the structural variations in

the crust of the basin are most intensive along the E-W section. Watts & Weissel (1975) shows the seismic reflection E-W cross sections across the Shikoku Basin (Figure 1.12). They argued that the morphology of the eastern crust to the Kinan Seamount Chain, which is thought to be the remnant of the spreading axis, shows increased roughness and complexity compared to the western crust. The seismic refraction experiments were conducted off the eastern coast of the Kii Peninsula (Murauchi et al., 1964; Murauchi et al., 1968) and off the southwest Shikoku Island (Yoshii et al., 1973). According to their results (Figure 1.13), the crust of the subducting Philippine Sea Plate in the east is thicker than the crust in the west.

1.5 Multi-channel Reflection Survey along the Nankai Trough

Many studies have been done on the landward slope of the Nankai Trough, and there can be seen the dominant structures of an accretionary prism, a bottom-simulating reflector (BSR), and a décollément. Multi-channel seismic reflection survey has provided the principal data for the studies on the structure and on the evolution process of the area (Kato, Sato & Sakurai, 1983). An extensive study of the structure of the accretionary prism was carried out by Ashi & Taira (1992) with the additional data from the IZANAGI backscattering measurement, DSDP (Leg 31, 58, 87) and Ocean Drilling Program (ODP Leg 131). They correlated the seismic reflection section with the IZANAGI backscattering image of the seafloor (Figure 1.14), and discussed the stereoscopic inner structure and its evolution. They interpreted the décollément as the water path at the contact between the overriding and the subducting plates (Figure

1.15). Ashi & Taira (1993) studied the thermal structure of the accretionary prism by the distribution of the BSR's, and suggested that the local fluid expulsion should be the major means of heat flow transfer. Okino & Kato (1995) discussed the variation of the geomorphic characteristics along the Nankai Trough with the wide collection of the SEABEAM bathymetry data.

1.6 Objective of This Study

As is seen through the previous sections, the Nankai Trough off Kii Peninsula is the place where the Philippine Sea Plate with heterogeneous structure along the trough axis subsides beneath the overriding plate at the rate of 43 mm/yr. And the contact of these two plates has generated big earthquakes with fairly regular periodic occurrences. The faults along the trough are composed of four mutually decoupled rupture zones.

There have been no seismic refraction survey except those cited above (Murauchi et al., 1964; Murauchi et al., 1968; Yoshii et al., 1973) along the Nankai Trough. The study area of Murauchi et al. (1964) and Murauchi et al. (1968) covered the Tonakai region (Zone C in Figure 1.3), but no deep structure has been available for the Nankaido area (Zone A and Zone B in Figure 1.3). The seismic refraction-reflection experiment was carried out by the group from four universities in 1994 in the region where the most prominent fault boundary is supposedly located. Our biggest concern is to ascertain whether a positive relationship is observed between earthquake activities and structural heterogeneities.

The artificial seismic sources of airgun shots and explosives were used and the data were collected by nineteen OBS's. Six OBS's among them were of digital type. In this study, a non-linear travel time inversion is newly developed and applied to the

experiment. The two-dimensional velocity structure model is obtained for one of the lines which runs parallel to the trough. The synthetic waveform computation method was also developed, and the waveforms are calculated with respect to the model obtained by the travel time inversions. They are compared with the observed waveforms to support the validity of the obtained velocity structure model.

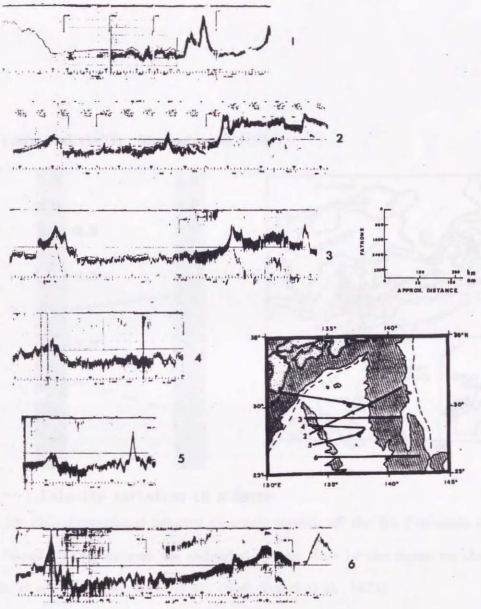

Figure 1.12: Seismic reflection profiles across the Shikoku Basin. Profiles 2-6 clearly show a contrast in the basement morphology between the western and eastern parts of the basin. (Watts & Weissel, 1975)

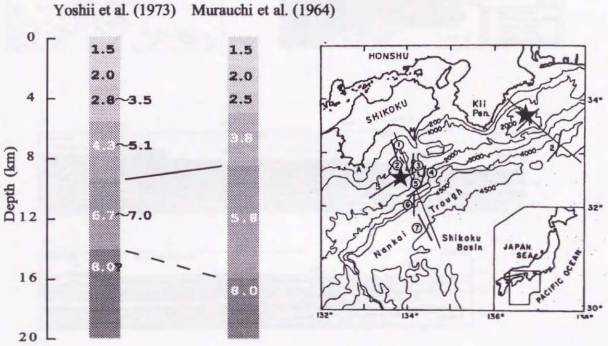

Figure 1.13: One-dimensional velocity structure models off the Kii Peninsula and the Shikoku Island. The locations are indicated by the stars in the figure on the right. (Murauchi et al., 1964; Murauchi et al., 1968; Yoshii et al., 1973)

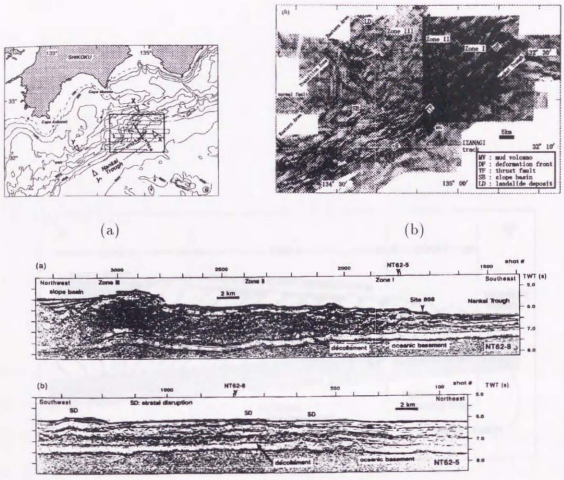

Figure 1.14: IZANAGI and reflection experiment off the Shikoku Island. (a) Bathymetry map. Box indicates experiment area. Cross-line is the location of multi-channel seismic reflection experiment, and the dotted line indicates the track of IZANAGI survey. (b) IZANAGI sidescan sonar bathymetric map. Topographic interpretation is presented. Zone I exhibits a rugged morphology which is parallel to the trough axis, Zone II is the place of low-reflectivity and covered by sediment, and Zone III shows high contrast lineaments and irregularly bounded configurations. (c) Multi-channel seismic reflection profiles along a cross-line. (Ashi & Taira, 1992)

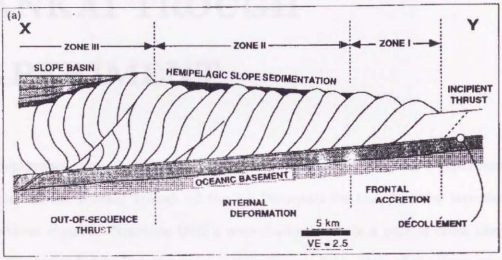

Figure 1.15: Structural diagram of accretionary prism. Zone I through III corresponds to the regions shown in Figure 1.14. (Ashi & Taira, 1992)

Chapter 2

NANKAI TROUGH EXPERIMENT

From September through October, 1994, a seismic refraction-reflection experiment was conducted at the Nankai Trough off the Kii Peninsula for the objective introduced in the previous chapter. Nineteen OBS's were deployed along a pair of cross lines with two OBS's being located at the intersection (Figure 2.1). One of the lines was ruled parallel to the trough axis, which is called "E-W line" hereafter. The E-W line spans 140 km and eleven OBS's were deployed along the line. 1602 airgun shots and 50 explosives were fired with the spacings of about 110 m and about 3 km, respectively. The other line, which runs perpendicular to the E-W line, is called "N-S line" hereafter and spans 150 km. Ten OBS's were deployed along this line, and 2203 airgun shots and 40 explosives were fired with the spacings of about 70 m and 3 km, respectively.

The study objective of the E-W line is to derive the crustal structure and to ascertain whether a positive relationship between earthquake activities and structural heterogeneities is observed, whereas that of the N-S line to derive a precise structural

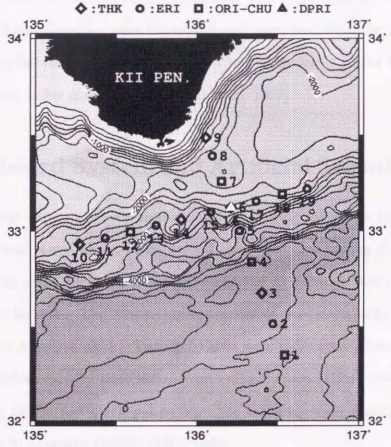

Figure 2.1: OBS locations in the 1994 Nankai seismic reflection-refraction experiment. Numbers are assigned to OBS's, and they are referred to as OBS's names in text.

picture of the subducting Philippine Sea Plate. This study is intended to a close investigation of the crustal structure along the Nankai Trough by applying the non-linear travel time inversion developed in this study from Mochizuki (1994). Also a numerical computation method to calculate waveforms is developed from the previous works

(Levander, 1988; Okamoto, 1991; Okamoto, 1994) so that it is easily applied to seismic experiments conducted in the ocean. Waveforms with respect to the model obtained by the travel time inversions were calculated and compared with the observed. The structure along the N-S line has been studied by Nishisaka at Chiba University and will be presented as his master's thesis (Nishisaka, 1997).

2.1 Onboard System and Artificial Seismic Sources

Airgun shots and explosives were used as artificial seismic sources in the experiment.

The airgun was towed about 30 m behind the vessel; the towing depth is 8 to 10 m. The capacity of its air chamber was 17 *l* and the air pressure was raised to about 10 Mpa before the shots. The shot-triggering operation was electrically controlled and synchronized to a quartz clock. The shot times were calibrated afterwards with the clock pulses transmitted by the Global Positioning System (GPS) satellites, as both shot-triggering pulses and clock pulses from the satellites were digitized and stored simultaneously in Magneto-Optical (MO) disks.

During the airgun operation, the single cannel hydrophone streamer (SCH) was towed from the tail of the vessel to observe the vertically propagating waves reflected at the seafloor and the sub-bottom reflectors.

Each explosive was 20 kg dynamite, except for two 440 kg shots along the NS line which, as being large enough to be recorded by the seismic stations on land, were dedicated to the landward crustal studies. Each 20 kg dynamite was packed in a corrugated carton, and the 440 kg shots were an assemblage of twenty-two boxes of 20 kg dynamite. Several buoys were towed by the wire from the vessel about 300 m behind for the 20 kg shots and about 1 km behind for the 440 kg shots, and the explosive was

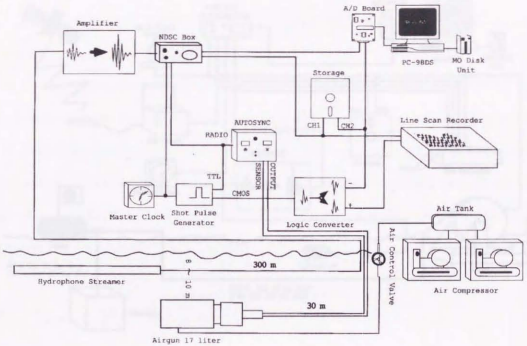

Figure 2.2: Settings of airgun, single channel hydrophone streamer and onboard system for airgun operation.

hung down from the buoys beneath the sea surface with a 30 m and a 100 m ropes, respectively. The shot-timing signals were transmitted through the electric cords which ran in the center of the wire.

Vessel locations were determined by GPS.

Figure 2.2 depicts the onboard data acquisition system for the airgun survey, and Figure 2.3 for the explosive survey.

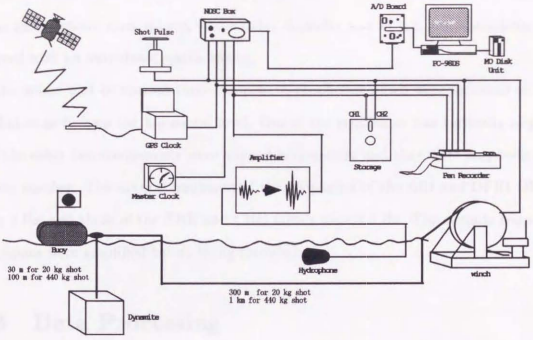

Figure 2.3: Settings of explosive and onboard system for explosion operation.

2.2 OBS Description

The OBS's were gathered from the following four organizations: Tohoku University (THK), Earthquake Research Institute, University of Tokyo (ERI), Chiba University (CHU), and Disaster Prevention Research Institute, Kyoto University (DPRI). The OBS's are different among the organizations. All OBS's were of a free-fall and pop-up type with acoustic-commandable sinker releasers. The CHU and DPRI OBS's were equipped with an analogue-to-digital converter and a digital recording system, whereas the OBS's of the other organizations with a direct analogue recording system which stores data on cassette tapes. Besides the recording system, they were equipped with an amplifier, a sensor unit, a time code generator, and a battery, so that they were fully

operative without assistance once being programmed. The whole system was housed in an anti-pressure glass sphere, whose outer diameter was 43 cm, and the sphere was covered with an anti-shock plastic casing.

The sensor unit comprised three-component geophones which were mounted on the gimbal so as to keep the horizontal level. One of the geophones was vertically aligned and the other two components were aligned horizontally and they were perpendicular to one another. The natural frequency of the geophones of the ERI and DPRI OBS's were 2 Hz, and those of the THK and CHU OBS's were 4.5 Hz. The outputs from the geophones were amplified before being recorded.

2.3 Data Processing

The location of each explosive shot was determined by the combination of the vessel position, the vessel heading and the wire length measured by observing the travel time of a direct water wave from a shot to the hydrophone receiver which was towed behind the vessel (Figure 2.3). The locations of the airgun shots were substituted by the vessel positions, since the distance between the gun and the vessel was close and about 30 m. The locations of the OBS's were determined by the least square fittings of the travel times of direct water waves from airgun shots to the OBS's with the information of the water depth measured on the SCH data.

The OBS clocks were calibrated to the GPS clock before analysis so that all the clocks used in the experiment were calibrated to the common reference time.

The data from the analogue OBS's were digitized with the sampling rate of about 100 Hz. The recorder's magnetic head was in most cases off-perpendicular to the track of the tape (Figure 2.4). As the result, the digitized data have to be calibrated to a

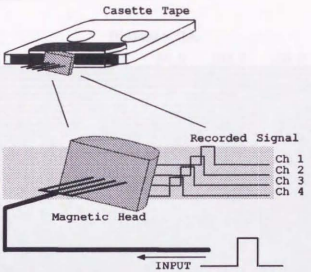

Figure 2.4: Slant magnetic head causes record-timing disparities among record channels.

reference channel. A series of clock pulses was input to all four channels simultaneously in order to measure the record-timing disparities among the channels. The measured disparities were calibrated before analysis.

2.4 Data Acquired through Experiment along the E-W Line

The data sets observed along the E-W line are shown in this section. Since this study is intended only to the E-W line, the data collected along the N-S line are not presented here.

2.4.1 SCH data

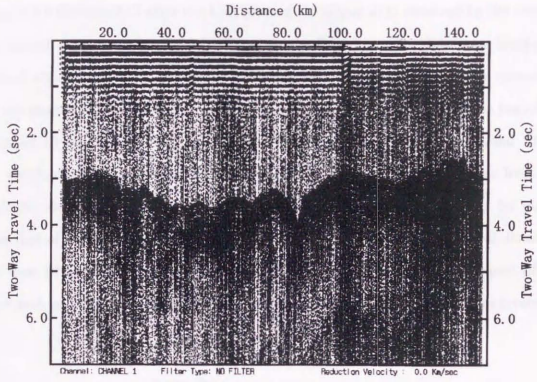

Figure 2.5: LSR plot of SCH data. Information on subbottom structure is not obtainable.

Figure 2.5 shows the data acquired by SCH. Each vertical trace corresponds to an airgun shot and is plotted so that a trace is marked when its amplitude exceeds a threshold level (called "LSR plot " hereafter). The seafloor topography can be accurately traced in the two way travel times, and converted to depth in meters by multiplying 1500/2 which is the water wave velocity divided by 2. Information on the subbottom structure is hardly obtainable on this record.

2.4.2 OBS data of airgun shots

Figures 2.6 through 2.13 show the LSR plots of the airgun data observed by the vertical component seismometers of the OBS's along the E-W line. The data were band-pass filtered whose frequency band was 5 $\sim$ 20 Hz. They were plotted after the correction for the geometrical spreading of energy. The first arrivals of P-wave can be traced up to about 10 km of the epicentral distance. Although the first arrivals beyond 10 km are visible on some OBS's records, their arrival times are later than those from the explosive shots of the same epicentral distances whose excited energy was far bigger than that of an airgun shot. Therefore, the airgun data with their epicentral distances less than 10 km were used to derive the velocity structure of the shallow part of the crust such as Layer 1 through Layer 2A by applying τ-p mapping and τ-sum inversion.

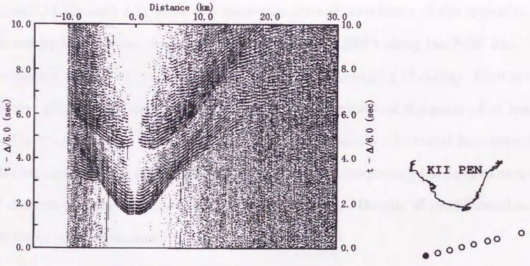

Figure 2.6: LSR plot of airgun data recorded by OBS#10

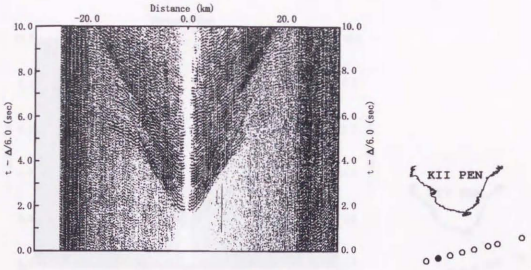

Figure 2.7: LSR plot of airgun data recorded by OBS#11

2.4.3 OBS observation of explosive shots

Figures 2.14 through 2.21 show the band-pass filtered waveforms of the explosive data observed by the vertical component seismometers of OBS's along the E-W line. They were plotted after the correction for the geometrical spreading of energy. First arrivals and later phases are clearly identifiable up to their epicentral distances of at least 60 km. The travel times of the P-wave first arrivals were used by the travel time inversions. Reflected arrivals were also taken into account while interpreting the layered structure and determining the depths of the velocity interfaces. Details of model-constructing procedures will be discussed in the next chapter.

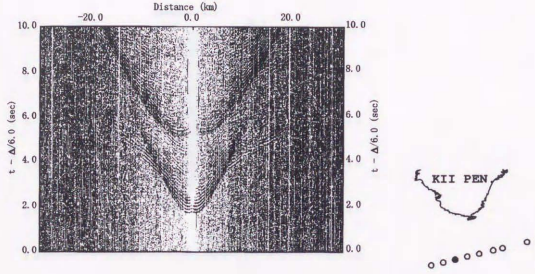

Figure 2.8: LSR plot of airgun data recorded by OBS#12

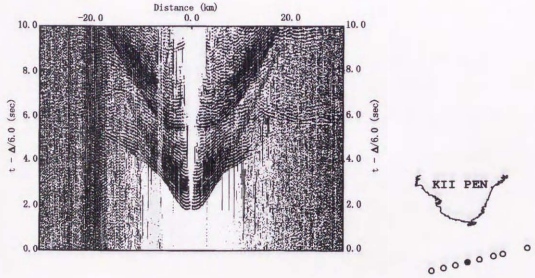

Figure 2.9: LSR plot of airgun data recorded by OBS#13

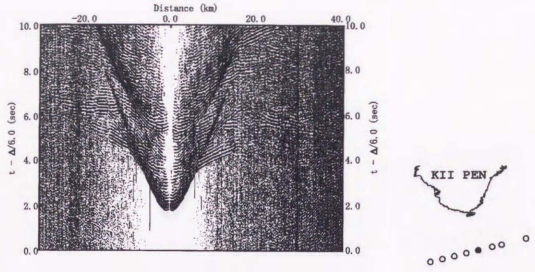

Figure 2.10: LSR plot of airgun data recorded by OBS#14

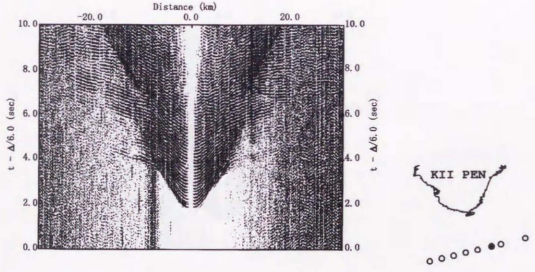

Figure 2.11: LSR plot of airgun data recorded by OBS#15

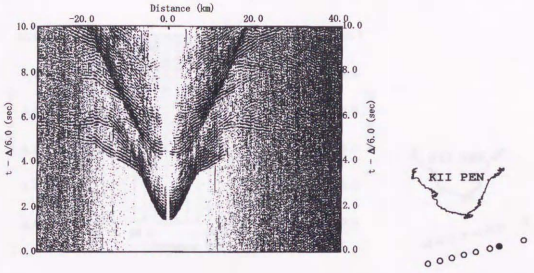

Figure 2.12: LSR plot of airgun data recorded by OBS#6

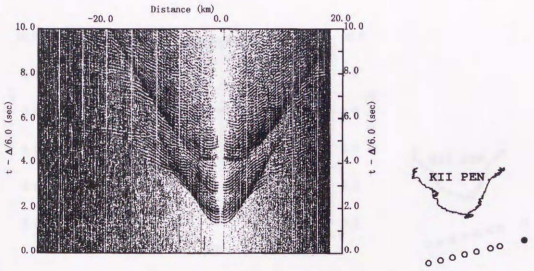

Figure 2.13: LSR plot of airgun data recorded by OBS#18

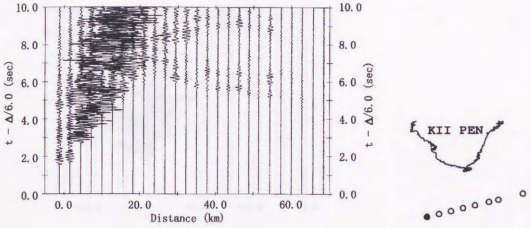

Figure 2.14: Observation of explosive data recorded by OBS#10

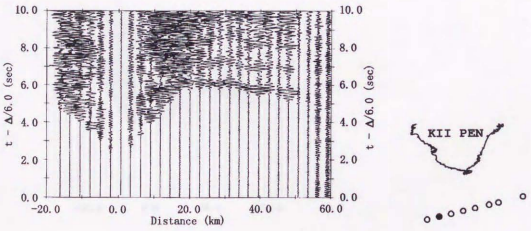

Figure 2.15: Observation of explosive data recorded by OBS#11

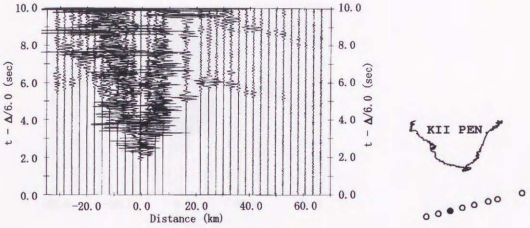

Figure 2.16: Observation of explosive data recorded by OBS#12

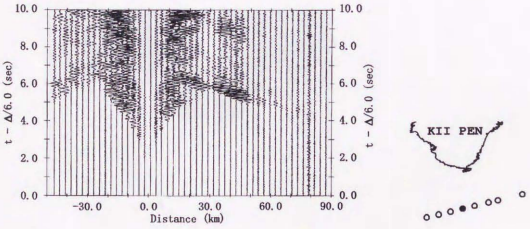

Figure 2.17: Observation of explosive data recorded by OBS#13

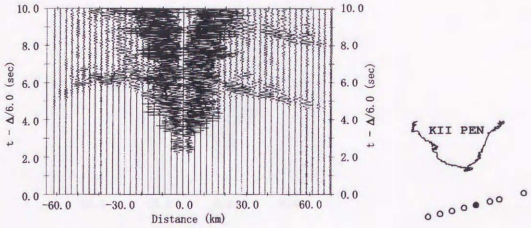

Figure 2.18: Observation of explosive data recorded by OBS#14

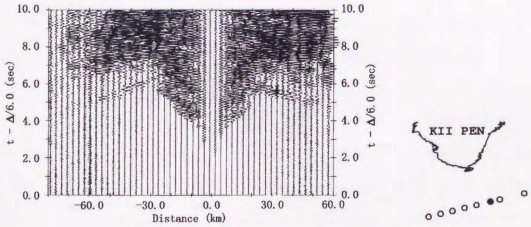

Figure 2.19: Observation of explosive data recorded by OBS#15

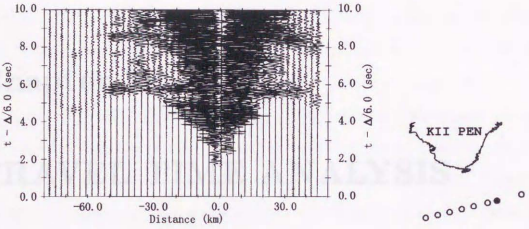

Figure 2.20: Observation of explosive data recorded by OBS#6

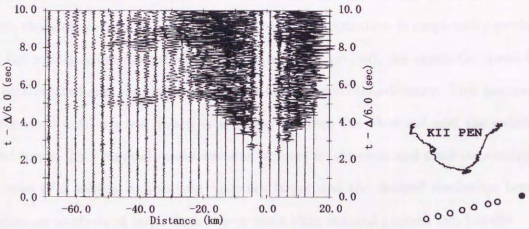

Figure 2.21: Observation of explosive data recorded by OBS#18

Chapter 3

TRAVEL TIME ANALYSIS

The trial-and-error forward modeling method has often been employed to derive two-dimensional velocity structure from interpreting seismic refraction-reflection data. In this method, synthetic travel-times are calculated by some ray-tracing method with respect to a velocity structure model, and they are compared with observed travel-times. By observing discrepancies between the calculated and the observed travel times, the location and the magnitude of model modification is empirically predicted, and the modification is applied. Once the model is revised, the synthetic travel-times are recalculated and compared again with the observed travel-times. This process will be repeated until a good match is attained between the observed and the calculated travel times. This manual model-revision process is laborious and time-consuming. As the scale of a seismic experiment becomes larger and the desired resolution becomes smaller, an analysis of large data sets is more than manual process can handle.

Tomographic travel time inversion can give interpretation according to a given criterion of travel-time residual convergence while taking the whole data sets into account at a time, and provides estimates of resolution and uncertainty of the resultant model.

In spite of these apparent advantages, applications have been limited to surveys with certain geometrical configurations, such as cross-hole or VSP (e.g., Ishii, Onishi, Aoki & Muraoka, 1995), in which the ray-coverage through a medium under survey is sufficient and the ray paths can be fairly approximated by straight lines. The fact that only a few applications of inversion can be seen in practical seismic refraction-reflection experiments reflects the difficulty of its application. The principal difficulty arises from the geometry of the experiment where the sources and the receivers are located at and near the surface, as well as from high nonlinearity of inverse problems, which is ascribed to the high heterogeneity of crustal velocity structure. In addition, most of inverse problems are under-determined and suffer from the insufficiency of data, which degrades the resolution of the problems. Data contamination by the intrinsic noise also causes uncertainty of the problems. While looking at computational difficulties, ray-tracing programs used in forward modeling are not suitably designed for application to seismic tomographic inversions. Mochizuki (1994) and Mochizuki, Kasahara, Sato, Shinohara & Hirata (1997) considered these problems and developed an inversion scheme suitable for seismic refraction surveys, then they applied the method to the 1992 Tsushima Basin seismic refraction-reflection survey.

Through the general course of analyzing seismic refraction-reflection data, the τ-sum inversion following the τ-p mapping of observed waveforms is attempted to derive one-dimensional velocity structures beneath all of the OBS's deployed in an experiment. Then they are gathered to construct a two-dimensional picture of the velocity structure throughout the medium. The two-dimensional velocity structure model is repeatedly revised until the final model is obtained employing the trial-and-error forward modeling, although definite criteria for convergence are not given. In this study, the course of the

analysis is reconsidered and improvements will be introduced to the method proposed by Mochizuki (1994) and Mochizuki et al. (1997). Finally, the velocity model is revised by applying a non-linear inversion scheme newly developed in this study, which includes recalculation of ray paths according to each model modification.

3.1 τ-p Mapping of Envelope Waveforms and τ-sum Inversion

The first step through the analysis is to obtain a one-dimensional velocity structure model beneath each OBS by applying τ-p mapping and τ-sum inversion to the observation (Diebold & Stoffa, 1981; Stoffa, Buhl, Diebold & Wenzel, 1981; Stoffa, 1989). In this study, τ-p mapping of the enveloped waveforms of the observation is introduced in order to improve the signal identification ability. The main conception of introducing the method is to avoid, on the τ-p mapping, excessive contribution from direct water waves with large amplitudes and to decrease cancelling out of amplitude due to a near π phase difference which can be caused by rough seafloor topography. Figure 3.1 explains how big amplitudes of direct water waves mask refracted/reflected waves with small amplitudes. When raw traces are summed along a constant slope, p, and the amount is projected at an intercept time, τ, the contribution from small amplitudes is concealed behind the oscillation of direct water waves with big amplitudes while τ advances. When enveloped traces are instead summed, the oscillation of big amplitudes are suppressed and the contribution from small amplitudes will become discernible. Figure 3.2 shows how rough seafloor topography causes a problem. As shown in Figure 3.2, if the roughness of the seafloor becomes equivalent to a half wavelength which

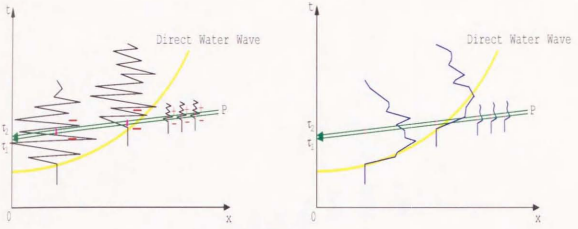

Figure 3.1: Water wave effect on τ-p mapping. (a) Amplitudes of raw signals are summed along a constant p and projected at τ. Oscillation of big water wave amplitudes conceal the contribution from small amplitudes of waves propagating through the crust. (b) Amplitude of enveloped signals are summed. Oscillation of water wave striding over the null amplitude is suppressed, and the contribution from small amplitudes becomes discernible.

corresponds to a phase difference by π, the sum of the amplitudes is cancelled out. However, if the enveloped traces are summed, this cancelation will not occur.

Taking envelope of a signal means abstraction of amplitude information from the original signal as it is called "instantaneous amplitude". Phase information is thus separated from the amplitude information, and it can be used as an individual data set. There are some implementation of using enveloped signals to make phase interpretation easier (e.g., Farnbach, 1975). In the study of Farnbach (1975), they used not only the amplitude information but the phase information altogether.

The envelope of a signal, $f(t)$, is calculated by taking a complex subtraction of its

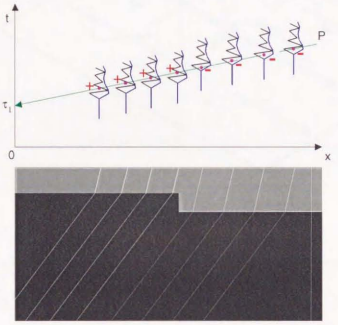

Figure 3.2: When roughness of the seafloor becomes equivalent to the half wavelength, near-π phase differences occur. This cause cancelation of amplitudes. When the enveloped waveforms are instead summed, this cancelation can be avoided.

Hilbert-transformed signal $F_H(t)$ from the original signal, as $f(t) - i\,F_H(t)$, which is called an analytic signal. If the instantaneous angular frequency of the analytic signal is ω, the analytic signal is expressed as $V(t)\exp^{i\omega t}$. The value $|V(t)|$ is the envelope of the signal and it is thus called the instantaneous amplitude. Figure 3.3 shows the

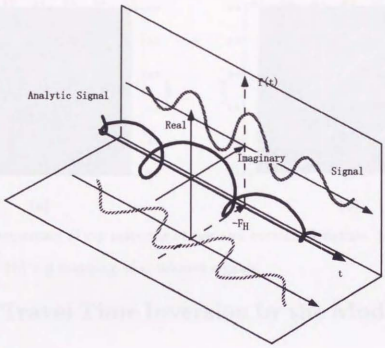

Figure 3.3: Relation among signal and its derivation by Hilbert transformation. Analytic signal is the sum of the signal, $f(t)$, and its Hilbert-transformed signal multiplied by $-i$, i.e., $-iF_H(t)$.

relation among a signal, its Hilbert-transformed signal, and the analytic signal.

Figure 3.4 shows an example of a general τ-p mapping on the left and a corresponding τ-p mapping of the enveloped signals on the right. Because the first arrivals from the airgun shots are observable only for the epicentral distances less than 10 km, not more than the shallow structure is derived by the τ-sum inversion.

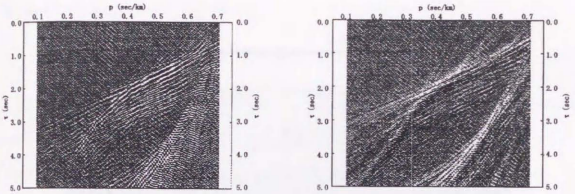

(a) (b)

Figure 3.4: Comparison of τ-p mapping of raw and enveloped signals. (a) τ-p mapping of raw signals. (b) τ-p mapping of enveloped signals.

3.2 2D Travel Time Inversion by the Modified Time-Term Method

After one-dimensional velocity structures beneath OBS's have been obtained, they are assembled to construct a two-dimensional velocity structure model of the shallower part of the crust. Then the modified Time-Term inversion was applied to roughly determine the interface geometries and P-wave velocities of layers assuming that each layer has a constant velocity. The result from this method can be referred to while constructing an initial velocity model for the more precise model revision-processes which are discussed in the later sections. A full description of the modified Time-Term method including synthetic tests of its applicability can be seen in Hino (1991), therefore, a brief explanation will be given here.

Suppose that a wave excited at a source is refracted, propagates along the interface whose velocity is V_n, and is received by a receiver (See Figure 3.5). The travel time of

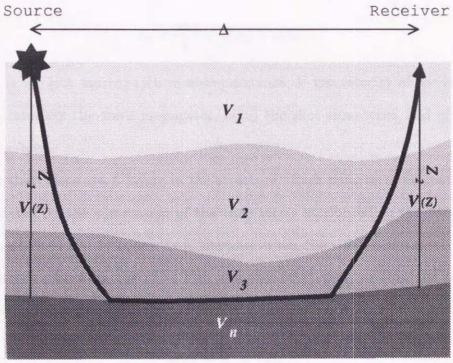

Figure 3.5: Geometry considered by the Time-Term method. V_i is the velocity in the ith layer, z_1 and z_2 are the depth of the interface of consideration measured at the location of the source and the receiver, respectively. Δ is the distance between the source and the receiver.

the ray, T, is approximately given by

$$\begin{aligned} T &= \frac{\Delta}{V_n} + \int_0^{z_1} \frac{\sqrt{V_n^2 - V(z_1)^2}}{V_n V(z_1)} dz_1 + \int_0^{z_2} \frac{\sqrt{V_n^2 - V(z_2)^2}}{V_n V(z_2)} dz_2, \\ &= \frac{\Delta}{V_n} + \text{shot time-term} + \text{station time-term}, \end{aligned} \tag{3.1}$$

where Δ is the source-receiver distance, $V(z)$ the velocity at the depth z, and z_1 and z_2 are the depths of the interface along which the wave propagates and are measured at the source location and the receiver location, respectively. The travel time, t_{ij}, between

the ith source located at x_i and the jth receiver at x_j, is given by

$$t_{ij} = \frac{\Delta_{ij}}{V} + a(x_i) + a(x_j), \tag{3.2}$$

where Δ_{ij} is the (ith source)-(jth receiver) distance, V the velocity of the layer along whose top interface the wave propagates, $a(x_i)$ the shot time-term, and $a(x_j)$ is the station time-term.

Suppose that there are L layers in the structure. Each time term evaluated at x is then calculated by the summation of the time terms attributed to the contributions from at most the $(L-1)$ layers as is the case when the wave propagates along the deepest interface between the $(L-1)$th and the Lth layers, so that the time term, $a(x)$, at the location x is expressed as

$$a(x) = \sum_{k=1}^{L-1} a^k(x), \tag{3.3}$$

where $a^i(x)$ is the fraction of the time-term ascribed to the ith layer. If the wave between the ith source and the jth receiver propagates along the interface between the lth and the $(l+1)$th layers, then the travel time is calculated as

$$t_{ij} = \frac{\Delta_{ij}}{V_{l+1}} + \sum_{k=1}^{l} a^k(x_i) + \sum_{k=1}^{l} a^k(x_j), \tag{3.4}$$

where V_{l+1} is the velocity of the $(l+1)$th layer.

Suppose that there are N sources and M receivers. Because the resolution of the interfaces need not be any finer than either of the shot or the receiver intervals at this early stage of analysis, the geometries of the interfaces can then be made represented by a smaller number of points than either N or M, which is now at kth interface set to P_k which can vary among the interfaces. Let us confine to the case that each interface is represented by P points at the same horizontal locations, x_p $(p = 1, 2, \cdots, P)$, for

simplicity. Time terms are evaluated at the representative points so that the time term attributed to the lth layer at the horizontal location, x_p, is expressed as $a^l(x_p)$. An arbitrary time term attributable to the lth layer at the horizontal location, x, is then calculated by a linear interpolation of the two time terms evaluated at the neighboring representative points, and it is expressed as

$$a^l(x) = \frac{x - x_p}{x_{p+1} - x_p} a^l(x_{p+1}) + \frac{x_{p+1} - x}{x_{p+1} - x_p} a^l(x_p). \tag{3.5}$$

The V_n dependence of the time terms (see equation (3.1)) is neglected to obtain approximated solutions of the layer thicknesses and velocities. Let us define the time term vector with $(l-1) \times P$ components, $\boldsymbol{a}^T$, as

$$\boldsymbol{a}^T = \left(a^1(x_1), \cdots, a^1(x_P); a^2(x_1), \cdots, a^2(x_P); \cdots; a^{(l-1)}(x_1), \cdots, a^{(l-1)}(x_P)\right). \tag{3.6}$$

Then with a coefficient vector, $\boldsymbol{c}_{ij}$, the equation (3.4) is written as

$$t_{ij} = \frac{\Delta_{ij}}{V_{l+1}} + \boldsymbol{c}_{ij} \cdot \boldsymbol{a}. \tag{3.7}$$

In the above equation, t_{ij} and Δ_{ij} are measurable values, and the components in the coefficient vector, $\boldsymbol{c}_{ij}$, are calculable. Having $N \times M$ observations of t_{ij} and Δ_{ij}, the system with $N \times M$ equations is formed. The unknowns in the system are V_l $(l = \{1 \ldots L\})$ and $\boldsymbol{a}$ which has $P \times (L-1) + 1$ components. The system can be solved by any numerical linear algebraic method. After solving the system, the thickness, $h^l(x_p)$, of the lth layer evaluated at x_p is approximately given by

$$h_p^l = a^l(x_p) \frac{V_l V_{l+1}}{\sqrt{V_{l+1}^2 - V_l^2}}. \tag{3.8}$$

The solution thus obtained is approximated quantities for the present. However, Hino (1991) confirms by synthetic tests that the method reconstructs true structure remarkably well.

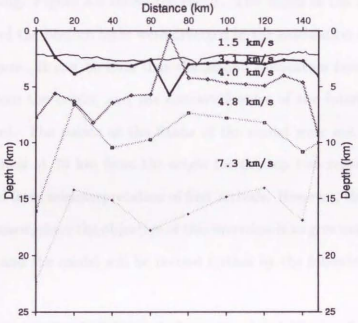

Figure 3.6: Result of the Time-Term analysis applied to the 1994 Nankai experiment. Interfaces are represented by the points plotted in the figure. Velocities of each layer are also shown. Concave feature of interfaces originates at 20 km east to the model origin and propagates easterly downward.

The method was applied to the Nankai experiment to obtain a rough picture of the two-dimensional velocity structure. The structure was given six layers including the

top water layer whose thickness and velocity were known. The top two subbottom interfaces were represented by sixteen points with 10 km spacing, the next two by nine points with 20 km spacing, and the bottom interface was represented by six points with 30 km spacing. Figure 3.6 shows the result. The depth of the bottom interface and the velocity of the bottom layer were diverged in the calculation and they are not shown on the figure. It can be seen that the second subbottom layer becomes thick at 30 km east from the origin, and the concave feature of the interfaces propagates easterly downward. The points at the flanks of the model were not properly solved. Anomalous solutions at 70 km from the origin for the top two representative points may be originated from misinterpretation of first arrivals. However, the result shall not be carefully discussed, since the objective of this inversion is to give only a rough sketch of the structure, and the model will be revised further by the following procedures.

3.3 Hybrid Model Revision by Trial-and-Error and Travel Time Inversion

After obtaining the results from the above processes, they are compiled to construct an initial model for further model revision by the more complex travel time inversion allowing velocity heterogeneity in each layer. The inversion scheme employed here is the modified version of the one developed by Mochizuki (1994). A brief explanation of the scheme is given in the following after Mochizuki (1994), Matsu'ura (1991) and Mochizuki et al. (1997).

The observation equation is written as

$$\boldsymbol{d} = \boldsymbol{f}(\boldsymbol{m}) + \boldsymbol{z}, \tag{3.9}$$

where $\boldsymbol{d}$ is the vector in the data space which consists of observations, $\boldsymbol{m}$ is the model parameter vector, $\boldsymbol{f}$ is the non-linear vector function relating the model parameters to the observations, and $\boldsymbol{z}$ is the vector expressing the noise contaminating the observations. If $\boldsymbol{z}$ is normally distributed around the average, $\mathbf{0}$, and is characterized by the variance-covariance matrix, $\boldsymbol{C}_d$, the probability density distribution, $p(\boldsymbol{d}|\boldsymbol{m})$, of the observations regarding the model, $\boldsymbol{m}$, is given by

$$p(\boldsymbol{d}|\boldsymbol{m}) = c \cdot \exp\left[-\frac{1}{2}\{\boldsymbol{d} - \boldsymbol{f}(\boldsymbol{m})\}^T \boldsymbol{C}_d^{-1} \{\boldsymbol{d} - \boldsymbol{f}(\boldsymbol{m})\}\right], \tag{3.10}$$

where c is a normalization factor and ^{T} denotes the transposition of a vector or of a matrix.

Suppose that the initial model, $\boldsymbol{m}_0$, is expressed with the error vector, $\boldsymbol{e}$, as

$$\boldsymbol{m}_0 = \boldsymbol{m}_{true} + \boldsymbol{e}, \tag{3.11}$$

where $\boldsymbol{m}_{true}$ is the true model, and that the errors are normally distributed around the average, $\mathbf{0}$, being characterized by the variance-covariance matrix, $\boldsymbol{C}_m$, then the probability density distribution, $p(\boldsymbol{m}_{true})$, of the true model, $\boldsymbol{m}_{true}$, is

$$p(\boldsymbol{m}_{true}) = c \cdot \exp\left\{-\frac{1}{2}(\boldsymbol{m}_0 - \boldsymbol{m}_{true})^T \boldsymbol{C}_m^{-1} (\boldsymbol{m}_0 - \boldsymbol{m}_{true})\right\}. \tag{3.12}$$

After applying Bayes' rule, $p(\boldsymbol{m}|\boldsymbol{d}) = c \cdot p(\boldsymbol{d}|\boldsymbol{m}) \cdot p(\boldsymbol{m})$, the probability density distribution of the true model regarding the observations, $p(\boldsymbol{m}_{true}|\boldsymbol{d})$, is expressed as

$$p(\boldsymbol{m}_{true}|\boldsymbol{d}) = c \cdot \exp\left\{-\frac{1}{2} s(\boldsymbol{m}_{true})\right\}, \tag{3.13}$$

where

$$s(\boldsymbol{m}) = \{\boldsymbol{d} - \boldsymbol{f}(\boldsymbol{m})\}^T \boldsymbol{C}_d^{-1} \{\boldsymbol{d} - \boldsymbol{f}(\boldsymbol{m})\} + (\boldsymbol{m}_0 - \boldsymbol{m})^T \boldsymbol{C}_m^{-1} (\boldsymbol{m}_0 - \boldsymbol{m}). \tag{3.14}$$

The estimated true model, $\boldsymbol{m}_{est}$, is obtained as the most probable model by seeking the solution which makes the objective index value, $s(\boldsymbol{m})$, the minimum: $p(\boldsymbol{m}|\boldsymbol{d})$ is made the maximum. Therefore, the system to be solved is written as

$$\frac{\partial s(\boldsymbol{m}_{est})}{\partial m_l} = 0, \qquad \text{for all } l. \tag{3.15}$$

The system of equations (3.15) is solved by appropriate numerical methods to obtain the estimated model, $\boldsymbol{m}_{est}$. If the inverse problem is linear or assumed to be linear, the system of equation (3.15) is perfectly expressed as

$$\boldsymbol{A}^T \boldsymbol{C}_d^{-1} \{\boldsymbol{d} - \boldsymbol{f}(\boldsymbol{m}_{est})\} + \boldsymbol{C}_m^{-1}(\boldsymbol{m}_0 - \boldsymbol{m}_{est}) = \boldsymbol{0}, \tag{3.16}$$

where $\boldsymbol{A}$ is the partial derivative matrix whose ijth component is $a_{ij} = \partial f_i(\boldsymbol{m})/\partial m_j$.

Figure 3.7 shows the flowchart of the inversion procedure. For the solution of a linearized inversion (equation (3.16)), the judgment of convergence is skipped and the result is obtained after executing the whole procedure once. In solving the above system, equation (3.15) or (3.16), are involved two major calculations. One of them is constructing a partial derivative matrix and the other is solving an inverse problem (shaded processes in Figure 3.7). Mochizuki (1994) assembled the methods for these major calculations to be suitable for seismic refraction experiments, and applied the scheme to the 1992 Tsushima Basin seismic experiment. They employed the Pseudo-Bending method for the ray-path calculation which is directly followed by construction of a partial derivative matrix, and the Conjugate-Gradient method for solving an inverse problem.

The scheme proposed by Mochizuki (1994) is modified to improve the stability, which makes the scheme fully applicable to non-linear inverse problems. The modification is

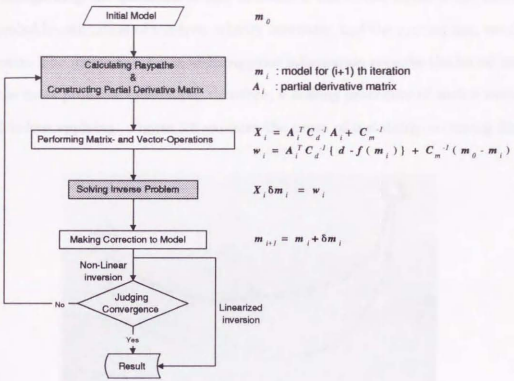

Figure 3.7: Flowchart of the inversion procedure. The major processes are shown by shaded rectangles.

made in the ray-path calculation in the scheme, and the method developed by Fujie (1996) is now employed. The method calculates the travel times of the first arrivals from a source to the grid points distributed through a medium with a constant spacing at a time, and also stores angles of incoming rays at the grid points. Then with the information of the incoming angles, it traces back a ray path from an arbitrary receiver to the source. The method is faster and more stable than the Pseudo-Bending method employed before by Mochizuki (1994), which makes the non-linear inversion scheme perfectly feasible to be applied. However, the non-linear inversion process

itself, disregarding the methods, is very unstable if the initial model is far from the most probable estimation of the true velocity structure, and the process may result in divergence. The inversion scheme utilizing prior information requires the initial model to be the most probable estimation, therefore, a seeking procedure of such a model is needed before applying. Figure 3.8 explains the cause of instability occurring during

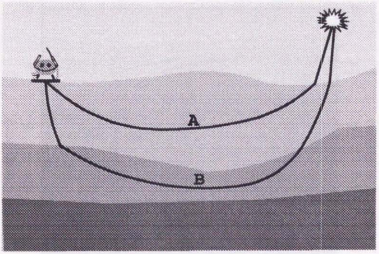

Figure 3.8: Origin of high non-linearity by ray-path leaping. See text for explanation.

the non-linear inversion procedure. Suppose the ray path connecting a source and a receiver is path A for a velocity model, and becomes path B after a model revision. The observation equation to calculate the travel time of the ith ray path is here expressed as

$$t_i = f_i(\boldsymbol{m}) = \int_{L_i} \frac{dl}{v}, \tag{3.17}$$

where the integration path, L_i, is taken along the ray path. If the ray paths often encounter as big changes as they leap among layers, it causes big alterations in the observation equations, and this may bring about a huge non-linearity of the problem.

This phenomenon must be restrained as much as possible. In this study, the following procedure is taken to provide the non-linear inversion process with a better velocity structure model. The P-wave velocities and the interface geometries were modified through the course.

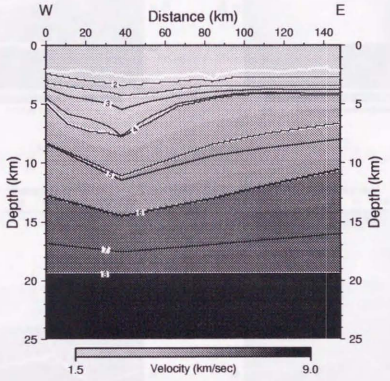

Figure 3.9: Starting model for inversion processes, compiled from the results of the preceding procedures. Velocities along contours whose interval is 0.5 km/s are superimposed. White lines indicate the velocity interfaces.

Figure 3.9 shows the starting model that was compiled from the results of the τ-sum inversion and the time-term inversion, and was refined to the first-degree by the trial-and-error travel time fitting procedure utilizing a ray-tracing method. Figure

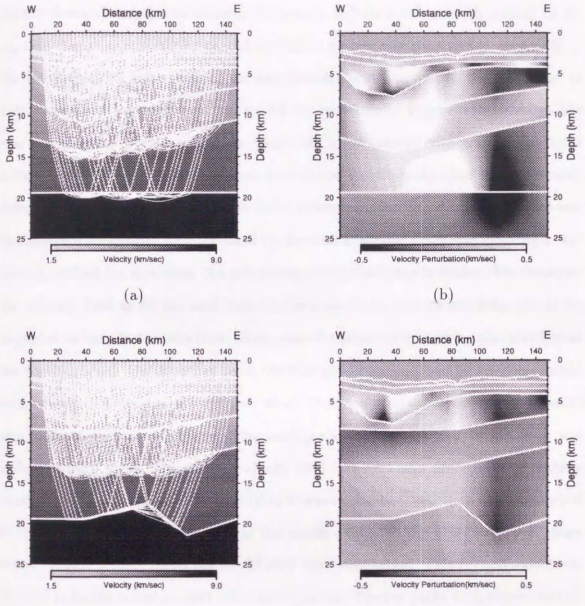

Figure 3.10: Example of hybrid model modification. Ray paths are calculated with respect to a starting model (a), and the partial derivative matrix is constructed. The inverse problem is solved to obtain the result (b). While utilizing the result, the model is further revised by the trial-and-error technique with a ray-tracing method (c). Ray paths and the partial derivative matrix with respect to this model is calculated, and the inverse problem will be solved (d).

3.10(a) shows the ray paths between the sources and the receivers with respect to the starting model, and then the partial derivative matrix was constructed according to the ray paths. As inferred from the ray coverage over the model, the resolution at both flanks and the bottom of the model are insufficient. Figure 3.10(b) shows the result of a linear inversion. On the result, the areas colored with white have faster velocities and those colored with black have slower velocities than the starting model, shown in the scale of ± 1 km/sec. To build a better model, the P-wave velocities and the interface geometries were modified by the trial-and-error technique utilizing a ray-tracing method incorporating the information from the linear inversion. For example, the velocity field at 80 km east from the western origin and 20 km deep should be upgraded to have faster velocities, which could be achieved by shifting the interface at the depth upward. On the other hand, the field at 110 km east and 20 km deep should be modified to have slower velocities, which then could be achieved by the opposite procedure to the preceding one. The interface at 30 km east and 10 km deep was shifted upward so as to make the velocity field faster. These procedures of shifting interfaces were accompanied by modifying P-wave velocities, and they were conducted in the trial-and-error manner so that the model explained the observed travel times better. Figure 3.10(c) shows the model after the modification. This revised model was thought to be the initial model to the next iteration. The ray paths with respect to this model were calculated, and the partial derivative matrix was constructed. The linear inverse problem was solved, and Figure 3.10(d) shows the result being shown in the same scale as the previous result. The velocity perturbations of the same magnitude as those of the previous result can no longer be evident at the locations where the interfaces and the velocities were modified. These procedures were repeated until a

good convergence of the velocity structure model was attained, i.e., the index value, $s(\boldsymbol{m})$, is made sufficiently small, so that the model could be served as the most likely velocity model to the non-linear inversion procedure.

The prior information was always incorporated in solving inverse problems. The standard deviations of the errors in the data space were determined by the signal readability of the first arrivals, and ranges from 25 msec for well-identified onsets and 100 msec for onsets with poor readability. The velocities of the shallower layers were thought to be well determined by the τ-sum inversion, and the standard deviation was set to 0.5 km/sec. The velocities of the deeper layers were not expected to vary, and the deviation was also set to 0.5 km/sec. The velocities of the intermediate layers are set to be 1.0 km/sec. Table 3.1 summarizes the standard deviation value in the model space.

3.4 Non-Linear Travel Time Inversion

The non-linear travel time inversion was made possible by employing the efficient and stable ray-path calculation method developed by Fujie (1996), since if the method is excessively keen to the model heterogeneity and the calculated ray paths are apt to diverge, it is impossible to construct an appropriate partial derivative matrix (equation 3.15). The method employed here can deal with any velocity structure, and calculates travel times and ray paths of first arrivals between any source-receiver pairs. It can be further developed so that it calculates the ray paths and travel times of later phases.

The vector function, $\boldsymbol{f}(\boldsymbol{m})$, is in fact non-linear. For a non-linear inverse problem, the system of equation (3.15) is solved with the initial model, $\boldsymbol{m}_0$, by an iterative scheme, within which the problem is treated to be linear under the assumption that

layer	1 (water)		2		3	
	top	bottom	top	bottom	top	bottom
Av. Vel. (km/s)	1.5	1.5	1.6	1.8	2.0	2.5
Std. Deviation (km/s)	0.0	0.0	0.0	0.0	0.5	0.5
layer	4		5		6	
	top	bottom	top	bottom	top	bottom
Av. Vel. (km/s)	2.8	3.8	4.0	4.4	5.0	5.3
Std. Deviation (km/s)	1.0	1.0	1.0	1.0	1.0	1.0
layer	7		8			
	top	bottom	top	bottom		
Av. Vel. (km/s)	6.7	7.2	8.0	8.6		
Std. Deviation (km/s)	0.5	0.5	0.5	0.5		

Table 3.1: Prior information in the model space.

the perturbations with respect to a reference model are small enough. The whole procedure shown in Figure 3.7 is repeated until the criteria for convergence is satisfied. The function, $\boldsymbol{f}(\boldsymbol{m})$, is Taylor-expanded with respect to an approximated model after k iterations, $\boldsymbol{m}_k$, and is written as

$$\boldsymbol{f}(\boldsymbol{m}) = \boldsymbol{f}(\boldsymbol{m}_k) + \boldsymbol{A}_k(\boldsymbol{m} - \boldsymbol{m}_k) + \cdots, \tag{3.18}$$

where $\boldsymbol{A}_k$ is the partial derivative matrix with respect to the model, $\boldsymbol{m}_k$. This expression is substituted to the equation (3.16) to obtain

$$\left(\boldsymbol{A}_k^T \boldsymbol{C}_d^{-1} \boldsymbol{A}_k + \boldsymbol{C}_m^{-1}\right)(\boldsymbol{m} - \boldsymbol{m}_k) = \boldsymbol{A}_k^T \boldsymbol{C}_d^{-1} \{\boldsymbol{d} - \boldsymbol{f}(\boldsymbol{m}_k)\} + \boldsymbol{C}_m^{-1}(\boldsymbol{m}_0 - \boldsymbol{m}_k). \tag{3.19}$$

The $(k+1)$th estimation for the true model, $\boldsymbol{m}_{k+1}$, is then obtained by solving the above equation (3.19) for $\boldsymbol{m}$. The model, $\boldsymbol{m}_{k+1}$, is written with the perturbation

vector, $\delta \boldsymbol{m}_k$, as

$$\boldsymbol{m}_{k+1} = \boldsymbol{m}_k + \delta \boldsymbol{m}_k, \tag{3.20}$$

and the equation (3.19) becomes

$$\left(\boldsymbol{A}_k^T \boldsymbol{C}_d^{-1} \boldsymbol{A}_k + \boldsymbol{C}_m^{-1}\right) \delta \boldsymbol{m}_k = \boldsymbol{A}_k^T \boldsymbol{C}_d^{-1} \left\{\boldsymbol{d} - \boldsymbol{f}\left(\boldsymbol{m}\right)\right\} + \boldsymbol{C}_m^{-1} \left(\boldsymbol{m}_0 - \boldsymbol{m}_k\right). \tag{3.21}$$

This expression is of the form, $\boldsymbol{X} \cdot \boldsymbol{v} = \boldsymbol{w}$, where $\boldsymbol{X}$ is a matrix, and $\boldsymbol{v}$ and $\boldsymbol{w}$ are vectors, and it is solved by applying the least-square criterion to obtain $\delta \boldsymbol{m}_k$. The iteration is repeated until the condition is met: either of the correction vector, $\delta \boldsymbol{m}_k$, or the index value to be minimized, $s\left(\boldsymbol{m}\right)$, becomes sufficiently small.

Figure 3.11 shows the velocity grid of the final model to which the non-linear inversion is applied. Two model parameters of P-wave velocities are assigned to each grid point: one parameter is for the layer upper to the point and the other for the layer lower to the point. A velocity at an arbitrary point is calculated by linear interpolation of the slownesses at the four neighboring points. The top two layers have the finer grid spacings in order to resolve the rough topography of the seafloor, and a standard deviation in the variance matrix, $\boldsymbol{C}_d$, of 0.0 km/sec is given to the model parameters in these layers (Table 3.1). There are 248 model parameters in these two layers, and they are numbered from 0 to 247 from the upper-left to the lower-right corners. Each of the next three layers has 26 model parameters, and a standard deviation of 0.5 km/sec is given to the parameters in the top of these layers which are numbered from 248 to 273, and that of 1.0 km/sec is given to the parameters in the bottom two layers which are numbered from 274 to 325. Each of the next three layers has 20 model parameters which are numbered from 326 to 385. A standard deviation of 1.0 km/sec is assigned to the grid points in the top layer, whereas that of 0.5 km/sec is given to the grid points in the other two layers.

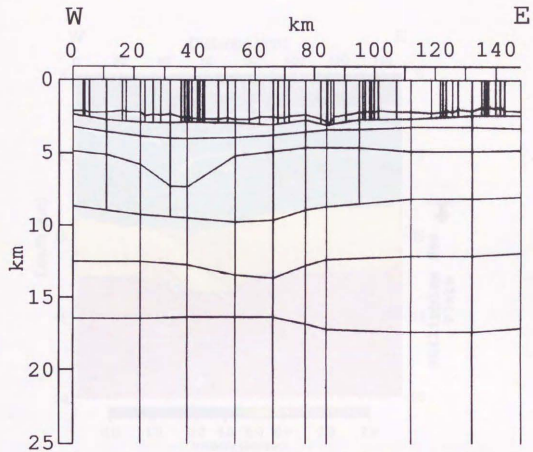

Figure 3.11: Velocity grid of the final model. Two model parameters of P-wave velocities are assigned to each grid point: one parameter is for the layer upper to the point and the other for the layer lower to the point. A velocity at an arbitrary point is calculated by linear interpolation of the slownesses assigned at the four neighboring grid points.

3.5 Results of Travel Time Inversion

Figure 3.12 shows the final result of the travel time inversion. The white lines on the figure depict the structural interfaces between layers. The velocity contours are also

superimposed with the annotations showing the velocities along the contours.

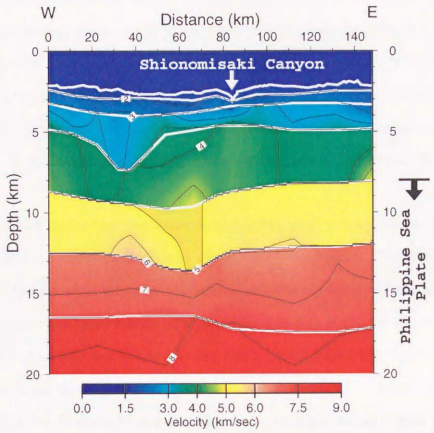

Figure 3.12: Result of non-linear inversion (The final model). Layers beneath the interface at 8 km deep belong to the subducting Philippine Sea Plate. Its crustal thickness changes abruptly at 70 km east to the model origin, and it becomes thicker in the east. Structural dividing line runs at the location, and it may reach the Shionomisaki Canyon. Material in the vicinity of the dividing line has slower velocities than the surrounding. Thick sediment exists at 30 km east to the model origin and 6 km deep.

The layers beneath the interface running at about 8 km deep belong to the subducting Philippine Sea Plate, and the interface running at about 17 km deep is interpreted as the

Moho interface of the Philippine Sea Plate. The thickness of the crust changes abruptly beneath the Shionomisaki Canyon located at 80 km east to the origin. The upper crust of the subducting plate at the place where the thickness changes is composed of the material with relatively slower velocity than the surrounding. It is interpreted as a structural dividing line runs almost vertically in the crust of the subducting plate at 80 km east to the origin. The line propagates upward until it may reach the Shionomisaki Canyon. A thick sedimentary layer is seen in the overriding plate at 30 km east to the origin.

Figure 3.13 shows how the index value, $s(\boldsymbol{m})$, and the root mean square (rms) of the travel time residuals decreased along with the model modifications. The model was modified for eight times by the hybrid procedure implementing the trial-and-error technique and the linear inversion as being discussed in the previous section. Then the non-linear inversion was applied to the ninth model which was regarded as the most probable initial model, and the final result was obtained. The index value, $s(\boldsymbol{m})$, and the rms for the final model are also plotted on the right end of Figure 3.13.

The estimation of the errors of the final model was evaluated under the assumption of linearity during the non-linear inversion procedure. The Taylor-expanded expression of the observation equation, equation (3.18), is substituted to equation (3.14) with respect to the final model neglecting the higher orders, and it is written as

$$\begin{aligned} s(\boldsymbol{m}) &= s(\boldsymbol{m}_{est}) + (\boldsymbol{m}-\boldsymbol{m}_{est})^T \left(\boldsymbol{A}_{est}^T \boldsymbol{C}_d^{-1} \boldsymbol{A}_{est} + \boldsymbol{C}_m^{-1}\right)(\boldsymbol{m}-\boldsymbol{m}_{est}) \\ &\quad - 2(\boldsymbol{m}-\boldsymbol{m}_{est})^T \left[\boldsymbol{A}_{est}^T \boldsymbol{C}_d^{-1} \{\boldsymbol{d}-\boldsymbol{f}(\boldsymbol{m}_{est})\} + \boldsymbol{C}_m^{-1}(\boldsymbol{m}_0-\boldsymbol{m}_{est})\right], \end{aligned} \tag{3.22}$$

where $\boldsymbol{A}_{est}$ is the partial derivative matrix with respect to the final model. Because the final model, $\boldsymbol{m}_{est}$, satisfies the equation (3.16), the third term of the above equation

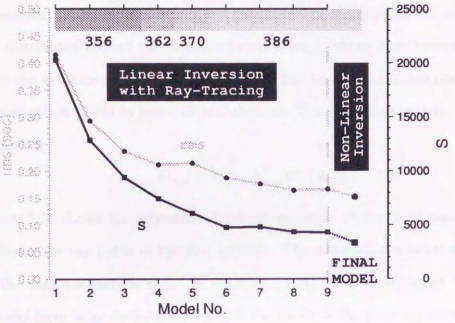

Figure 3.13: Index value, s, and rms along the model modification. Both decrease with model modifications. Model was revised eight times and the non-linear inversion was applied to the ninth model. Values of s and rms for the final model are plotted on the right end.

disappears so that the equation becomes

$$s(\boldsymbol{m}) = s(\boldsymbol{m}_{est}) + (\boldsymbol{m} - \boldsymbol{m}_{est})^T \left(\boldsymbol{A}_{est}^T \boldsymbol{C}_d^{-1} \boldsymbol{A}_{est} + \boldsymbol{C}_m^{-1} \right) (\boldsymbol{m} - \boldsymbol{m}_{est}) . \tag{3.23}$$

This expression is substituted to the equation (3.13) and the probability density distribution of the true model with respect to the observation is given by

$$p(\boldsymbol{m}_{true}|\boldsymbol{d}) = c \cdot \exp \left\{ -\frac{1}{2} (\boldsymbol{m}_{true} - \boldsymbol{m}_{est})^T \boldsymbol{C}_{true}^{-1} (\boldsymbol{m}_{true} - \boldsymbol{m}_{est}) \right\}, \tag{3.24}$$

with

$$\boldsymbol{C}_{true} = \left(\boldsymbol{A}_{est}^T \boldsymbol{C}_d^{-1} \boldsymbol{A}_{est} + \boldsymbol{C}_m^{-1} \right)^{-1}. \tag{3.25}$$

The equation (3.24) indicates that the parameters of the true model, $\boldsymbol{m}_{true}$, are normally distributed around the estimated model, $\boldsymbol{m}_{est}$, whose distribution is characterized by the variance-covariance matrix, $\boldsymbol{C}_{true}$. The true model is described completely by the equation (3.24) in terms of probabilities. The resolution matrix, $\boldsymbol{R}_{true}$, can be calculated by

$$\boldsymbol{R}_{true} = \boldsymbol{C}_{true} \boldsymbol{A}_{true}^T \boldsymbol{C}_d^{-1} \boldsymbol{A}_{true}. \tag{3.26}$$

Figure 3.14 shows the estimated standard deviation of the final model and Figure 3.15 shows the ray paths of the first arrivals. The standard deviation was calculated from the variance matrix, $\boldsymbol{C}_{true}$, in equation (3.24). The velocities at both flanks of the model have large deviations, which is the result of the poor ray coverage at those places (Figure 3.15). A fairly large deviation is seen in the sedimentary layer centered beneath the Shionomisaki Canyon at 80 km east to the origin and 4 km deep. This can be explained by the ray-path geometry with respect to the final model. The directions of the paths propagating through the region are almost vertical, and this uniqueness causes singularity in the inverse problem. To the contrary, there are several turning rays whose bottom points are located in the other regions in the same layer. Bad readability of the travel-times of the first arrivals which were generated by the shots located above the canyon also causes uncertainty of the result. As will be discussed in Section 4.6, the amplitude of the shots fired above the canyon is small, and identification of these first arrivals is difficult for those shots. However the velocities at other locations throughout the medium are well constrained. The largest velocity deviation is 0.5 km/sec along the velocity interface at 12 km deep. The velocity deviations of the thick sediment is

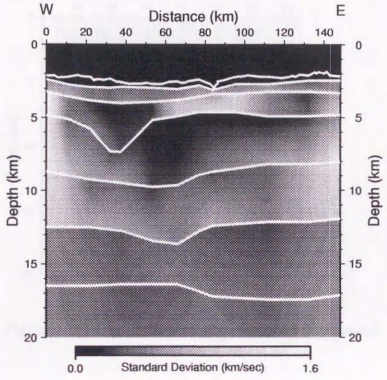

Figure 3.14: Standard deviations of the final model. Large deviations are observed along both flanks of the model and in the sediment at 80 km east to the model origin. Velocities are well constrained at other parts. The largest deviation in the model except for the regions mentioned above is 0.5 km/sec along the velocity interface at 12 km deep.

remarkably small and less than 0.1 km/sec. The velocities along the Moho interface of the subducting Philippine Sea Plate is constrained by 0.4 km/sec. The overall average deviation through the medium is about 0.3 km/sec.

Figure 3.16 shows the resolution matrix calculated from equation (3.26). Magnitude of the matrix components are shown in the scale of ± 2. As is described in the previous

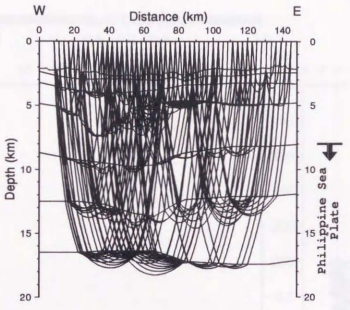

Figure 3.15: Ray paths with respect to the final model.

section, there are 386 model parameters. The most ideal resolution matrix is described as the diagonal components are one and otherwise null. The first 248 parameters belong to the first two layers, the velocity structure of which is considered to be constrained well by the τ-p mapping and τ-sum inversion, and the matrix components are all null. Some of the diagonal components are less than 0.5: their resolutions are poor. This is because they correspond to the parameters at the flank of the model where the ray-coverage is poor. It can be said that the non-linear inverse problem is well resolved.

3.6 Gravity Anomaly

The gravity anomaly expected from the obtained model was calculated by the 2D computation method proposed by Talwani, Worzel & Landisman (1959), and it was

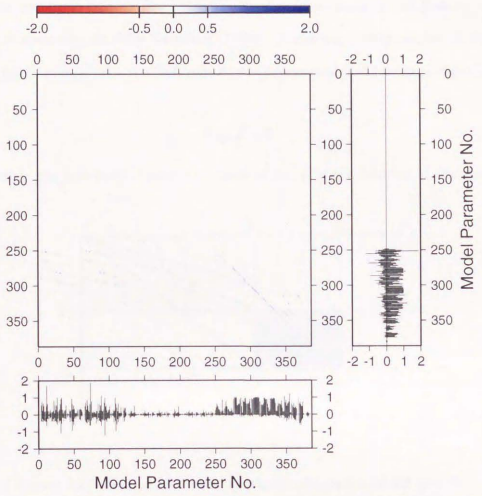

Figure 3.16: Resolution matrix obtained by equation (3.26). Magnitude of matrix components are shown in the scale of ± 2. There are 386 model parameters numbered from 0 to 385 in the order from upper-left to lower-right in each layer (see text in previous section).

compared with the observation compiled by Fukuda (1990).

The model was discretized into rectangles with an arbitrary dimension. Each rectangle is assigned an average density which is converted from an average P-wave velocity

inside the rectangle into its corresponding density by looking up the P-wave velocity-density relation compiled by Hamilton (1978). According to Talwani et al. (1959), a vertical gravitational contribution from a two-dimensional body measured at the origin is

$$2G\rho \oint z d\theta, \tag{3.27}$$

where G is the universal constant of gravitation, ρ is the density of the body, θ is

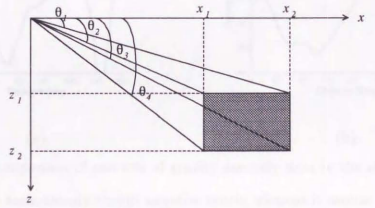

Figure 3.17: Geometry for the synthetic calculation of 2D gravity.

measured clockwise from the horizontal axis, z is measured positive downward, and the line integral is taken along its periphery. When the body is represented by a rectangle as it is the case here, the above expression (equation 3.27)evaluated at the origin can be expressed in a simpler form for a rectangle defined by the x values, x_1 and x_2 ($x_1 < x_2$), and the z values, z_1 and z_2 ($z_1 < z_2$) (Figure 3.17):

$$2G\rho \left\{ z_1 (\theta_2 - \theta_1) + z_2 (\theta_4 - \theta_3) + x_2 \log_e \frac{\cos\theta_2}{\cos\theta_3} - x_1 \log_e \frac{\cos\theta_3}{\cos\theta_4} \right\}, \tag{3.28}$$

where θ is measured clockwise from the horizontal axis at the origin, and its subscript is counted clockwise from the left-top corner. It is assumed in the calculation that the

one-dimensional structure beneath either flank of the model continues to infinity in respective direction, which is later referred to as the model termination effect.

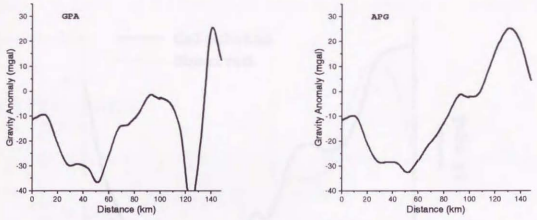

(a) (b)

Figure 3.18: Comparison of two sets of gravity anomaly data in the study area. GPA data set has an anomalously abrupt negative notch, whereas it cannot be seen in APG data set. (Fukuda, 1990)

Two individual data sets of gravity anomaly were compiled by Fukuda (1990). One of them was compiled using mainly the gravity data with additional information from the altimetry data (GPA) (Figure 3.18.(a)), and the other using mainly the altimetry data with additional information from the gravity data (APG)(Figure 3.18.(b)). There is a big discrepancy between the data sets in the eastern part of the region of this study, although a good match is seen in other parts. The GPA data set shows a huge negative anomaly at 120 km east to the model origin. This huge negative anomaly can be ascribed to some unavoidable errors in the surface ship gravity data (personal communication with Fukuda, 1996), so the result of the synthetic calculation is compared

with the APG data set (Figure 3.19).

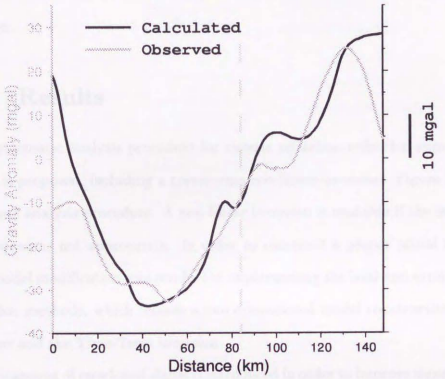

Figure 3.19: Comparison of gravity anomaly between calculation and observation. Calculated gravity is shown with thick solid line, and observation with thin solid line. They match considerably well, while the standard deviation of the observational error is 10 mgal in this region.

Although the error estimation of the observed gravity anomaly is about 10 mgal in the region, a remarkably good match is seen throughout the model region except at both ends where the contribution from the model termination effect is not negligible. The

gravity anomaly along the experiment line shows negative to positive variation from east to west, and this variation is explained by the lateral structural heterogeneity of the crust of the subducting Philippine Sea Plate (Figure 3.12). The position of the steepest inclination of the anomaly coincides with the location of the Shionomisaki Canyon.

3.7 Results

The systematic analysis procedure for seismic refraction-reflection experiments in the ocean is proposed, including a travel-time non-linear inversion. Figure 3.20 shows the proposed analysis procedure. A non-linear inversion is unstable if the initial model for the process is not appropriate. In order to construct a proper initial model, the hybrid model modification was conducted implementing the trial-and-error and linearized inversion methods, which follows a two-dimensional model construction by τ-sum inversions and the Time-Term inversion.

τ-p mapping of enveloped signal is introduced in order to improve signal identification ability. After the τ-p mapping, τ-sum inversion is applied to derive one-dimensional velocity structure of the shallow crust beneath each OBS. The one-dimensional structure models are gathered to obtain a two-dimensional picture of the shallow crust. Time-Term inversion is next applied to obtain a two-dimensional rough sketch of the structure including the deeper crust. The resultant structure model is modified to the first-degree by the trial-and-error travel time fitting method, and with this model as the starting model, the hybrid model modification by the trial-and-error and linear inversion methods are applied. After obtaining an appropriate initial model, the non-linear inversion is finally applied and the final model is derived.

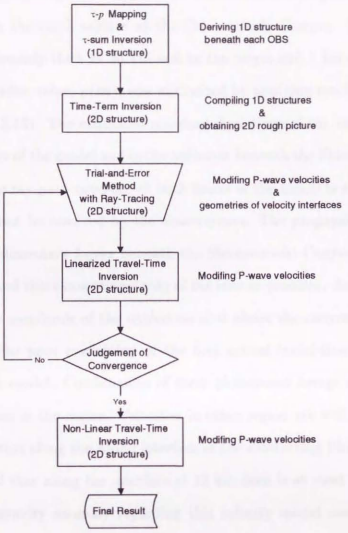

Figure 3.20: Flowchart of the travel-time analysis proposed in this study.

A two-dimensional precise velocity structure model was obtained for the E-W line of the 1994 Nankai Trough seismic experiment by applying the tomographic non-linear inversion to the OBS observations (Figure 3.12). The thickness of the crust belonging to the subducting Philippine Sea Plate changes beneath the Shionomisaki Canyon at 70 km east to the origin. It is interpreted as a structural dividing line runs almost vertically

in the crust of the subducting Philippine Sea Plate. The dividing line may propagate upward and reach the earth surface at the Shionomisaki Canyon. The sedimentary layer becomes extremely thick at 30 km east to the origin and 7 km deep.

The objective index value, $s(\boldsymbol{m})$, was minimized by applying non-linear travel time inversion (Figure 3.13). The estimated standard deviations of the velocities are fairly large at both flanks of the model and in the sediment beneath the Shionomisaki Canyon (Figure 3.14). The ray-path coverage at both flanks of the model is not sufficient, and the velocities cannot be resolved by the observations. The propagation directions of the rays in the sedimentary layers beneath the Shionomisaki Canyon is almost vertical(Figure 3.15), and this causes singularity of the inverse problem. As will be discussed in section 4.6, the amplitude of the explosives shot above the canyon is much smaller than expected. The poor readability of the first arrival travel-times may cause the uncertainty of the model. Combination of these phenomena brings about fairly large standard deviations in the region. Velocities in other region are well constrained, and the average deviation along the Moho interface of the subducting Philippine Sea Plate is 0.4 km/sec, and that along the interface at 12 km deep is at most 0.5 km/sec.

The synthetic gravity anomaly regarding this velocity model match the observed gravity anomaly remarkably well, which supports the validity of the model. The standard deviation of the gravity observation is about 10 mgal in the region, and the calculated and the observed values agree to each other within the deviation in spite of two-dimensionality of the calculation. The anomaly shows positive values in the east to the Shionomisaki Canyon and negative in the west. The structural variation in the shallower layers belonging to the overriding plate could not explain the peak-to-peak difference of the gravity anomaly, and it is necessary to include the thickness change

in the crust belonging to the subducting Philippine Sea Plate.

Chapter 4

FINITE DIFFERENCE CALCULATION

Many of seismic refraction-reflection researches conducted in the ocean are yet confined to travel time analysis studies. There has been hesitation to discuss in detail seismic waveforms recorded by OBS's because enough reliability on the data cannot be expected while the data are recorded on a cassette tape by a direct analogue recorder whose dynamic range is 40 dB. Also many physical properties such as OBS's state of coupling to the seafloor remain unknown. However, much instrumental improvement has been achieved by equipping an A/D converter to an OBS and digital recording has become possible. As the result, the dynamic range is broaden to 116 dB, and the accuracy of data sampling is greatly improved. Therefore, sufficient reliability on the data is attained which makes discussion on waveforms feasible including studies on the physical unknowns.

After a velocity structure model is derived for a two-dimensional experiment line, synthetic waveforms can be calculated with respect to the model. They can be calcu-

lated according to the ray theory, as such a computational code is already included in the package which deals with two-dimensional velocity structure modeling, e.g, SEIS83 (Červený, Molotkov & Pšenčík, 1977; Červený & Pšenčík, 1983). However this method cannot deal with dispersions. Some other attempts have been made for waveform calculations by using the reflectivity method (e.g., Fuchs & Müller, 1971; Spudich & Orcutt, 1980). However, since the method handles only one-dimensional velocity structure, research areas have been restricted in places without much heterogeneity.

The finite difference method is the best to compute synthetic waveforms for heterogeneous structure, solving numerically the wave equations at the grid points distributed in a medium. It is theoretically possible for the method to deal with any structure. Velocity structure to be studied in seismic refraction-reflection surveys is often very complicated and far from homogeneous layering structure. However as the heterogeneity increases, it needs a finer grid-point spacing and more computational time. The computational time increases linearly at the same proportion along with the model dimensions and the waveform length in time. However it increases at eight time as much proportion as the maximum source frequency. So the choice of the source frequency must be the first concern.

In this chapter, an application of the finite difference calculation of waveforms to the velocity structure of the Nankai Trough obtained in the previous chapter is discussed. Then compensation for seismometer's natural frequency, attenuation, a point source and the energy transmission fluctuation are considered. Finally, the calculated synthetic seismograms are compared with the observation. The calculated waveforms show quite a good match with the observation except for the reflected waves.

4.1 Method: Fourth-Order Calculation

Explicit finite difference schemes require huge computer memory to model practical refraction-reflection experiments, hence computationally expensive. Also it has been studied that there arises computational instability at the liquid-solid interface, and some attempts have been made to avoid this instability: Stephen (1983) introduced a ramp discontinuity between a liquid-solid interface, whereas Okamoto & Miyatake (1989) adapted the acoustic equation to a liquid medium and the elastic wave equations to a solid medium and matched the boundary conditions explicitly. As Levander (1988) tested the case with the staggered-grid finite difference scheme developed by Madariaga (1976), he claimed the staggered-grid scheme allowed sharp acoustic-elastic discontinuities without the need for special boundary conditions. It is necessary to have a water layer and subbottom crustal layers to model seismic refraction-reflection experiments conducted in the ocean, and the staggered-grid finite-difference method is considered to be most suitable.

The staggered-grid finite-difference scheme was first developed by Madariaga (1976) to solve the first-order coupled elastic equations of motion and constitutive laws expressed in particle velocities and stresses. In a two-dimensional Cartesian system, the P-SV equations of motion are

$$\rho \frac{\partial u_t}{\partial t} = \frac{\partial \tau_{xx}}{\partial x} + \frac{\partial \tau_{xz}}{\partial z} \tag{4.1}$$

and

$$\rho \frac{\partial w_t}{\partial t} = \frac{\partial \tau_{xx}}{\partial x} + \frac{\partial \tau_{zz}}{\partial z}; \tag{4.2}$$

and the constitutive laws for an isotropic medium are

$$\tau_{xx} = (\lambda + 2\mu) \frac{\partial u}{\partial x} + \lambda \frac{\partial w}{\partial z}, \tag{4.3}$$

$$\tau_{xx} = \mu \left(\frac{\partial u}{\partial z} + \frac{\partial w}{\partial x} \right), \tag{4.4}$$

$$\tau_{zz} = (\lambda + 2\mu) \frac{\partial w}{\partial z} + \lambda \frac{\partial u}{\partial x}, \tag{4.5}$$

where u and w are the displacements, u_t and w_t are the particle velocities in the x and the z directions, respectively, τ_{ij} are the stresses, λ and μ are the Lame's constants, and ρ is the density.

The scheme was further developed by Viriuex (1984) and Viriuex (1986) for modeling SH and P-SV waves in a two-dimensional Cartesian system. Their finite-difference operators were second-order accurate in time and space. Levander (1988) developed the scheme and introduced the finite-difference operators with the forth-order accuracy in space and second-order accuracy in time to model P-SV waves in a two-dimensional Cartesian system.

Figure 4.1 shows how the physical parameters are defined on the staggered grid points. The grid is also staggered in time such that the velocities and the stresses are updated with the time difference of the half sampling step, $\Delta t/2$. Levander (1988) argued that the scheme is stable about Poisson's ratio and that grid dispersion is small. The grid points in a medium must be sampled at 5 grid-points/shortest-wavelength for the forth-order scheme in contrast to 10 grid-points/shortest-wavelength for the second-order scheme. The use of higher-order accurate finite-difference approximations reduces the spatial sampling and hence computational time.

The top of structure to be modeled is bounded by the free surface; $\tau_{zz}|_{z=0} = 0$ and $\tau_{xz}|_{z=0} = 0$. These boundary conditions are satisfied merely by extending one grid above the surface, $z = 0$ (Alterman & Loewenthal, 1972). The other surrounding sides are bounded by the absorbing condition (Clayton & Engquist, 1977) and some grid

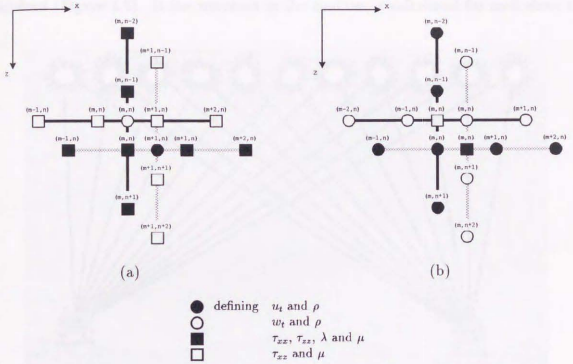

Figure 4.1: Staggered grids in the finite difference calculation. (a) Velocity stencil. A velocity is updated by the stresses defined at the surrounding four staggered grids in space at $\Delta t/2$ before in time. (b) Stress stencil. A stress is updated by the velocities defined at the surrounding four staggered grids in space at $\Delta t/2$ before in time.

points are used for damping reflections (Levander, 1985).

4.2 Reciprocity

In the seismic refraction-reflection experiment conducted in the ocean, the artificial seismic sources are located at the sea surface, and OBS's are deployed on the ocean bottom. A few hundred explosive shots and/or more than one thousand airgun shots are fired in contrast to the number of the receivers, which is generally less than one

hundred (Figure 4.2). If the wavefield in the medium is calculated for each shot, it

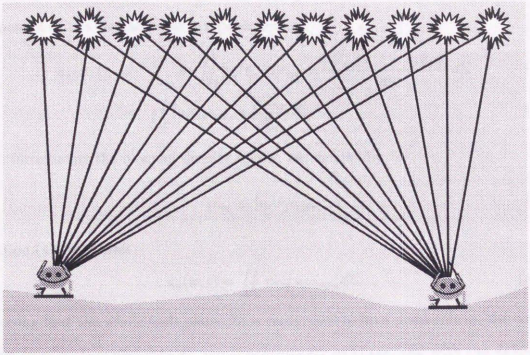

Figure 4.2: Source-Receiver geometry – Effectiveness of reciprocity. The number of sources located at the sea surface reaches a few thousands, whereas the number of receivers are less than a hundred. Wavefield calculation for each source is not realistic.

is computationally too expensive or even not feasible especially for airgun shots. The number of the receivers is much less than the number of the sources, and it is necessary to incorporate the special reciprocal relation for the source and the receiver;

$$G_{nm}(\boldsymbol{\xi}_2, \tau; \boldsymbol{\xi}_1; 0) = G_{mn}(\boldsymbol{\xi}_1, \tau; \boldsymbol{\xi}_2, 0), \tag{4.6}$$

where $G_{in}(\boldsymbol{x}, t; \boldsymbol{\xi}, \tau)$ denotes the elastodynamic Green function representing the ith component of displacement response at general $(\boldsymbol{x}, t)$ to the unit impulse applied at $\boldsymbol{x} = \boldsymbol{\xi}$ at $t = \tau$ in the n-direction (Aki & Richards, 1980, eq. (2.39)). With the

condition that the traction and the Green function are continuous on the surface of the elastic medium, Σ, for the spontaneous rupture discontinuity, $[\boldsymbol{u}(\boldsymbol{\xi},\tau)]$, the nth component of the displacement is represented as

$$u_n(\boldsymbol{x},t) = \int_{-\infty}^{\infty} d\tau \iint_{\Sigma} [u_i(\boldsymbol{\xi},\tau)] c_{ijpq} \nu_j \frac{\partial G_{np}(\boldsymbol{x},t-\tau;\boldsymbol{\xi},0)}{\partial \xi_q} d\Sigma \tag{4.7}$$

$$= \iint_{\Sigma} [u_i] \nu_j c_{ijpq} * \frac{\partial G_{np}}{\partial \xi_q} d\Sigma \tag{4.8}$$

With introducing the moment density tensor, $\boldsymbol{m}$, defined by

$$m_{pq} \equiv [u_i] \nu_j c_{ijpq}, \tag{4.9}$$

equation (4.8) becomes

$$u_n(\boldsymbol{x},t) = \iint_{\Sigma} m_{pq} * G_{np,q} d\Sigma. \tag{4.10}$$

Assuming that the whole fault plane, Σ, is recognized to be a point source, the contribution from surface elements $d\Sigma$ are approximately in phase, and with the definition of the moment tensor

$$M_{pq} = \iint_{\Sigma} m_{pq} d\Sigma = \iint_{\Sigma} [u_i] \nu_j c_{ijpq} d\Sigma, \tag{4.11}$$

equation (4.10) is expressed as

$$u_n(\boldsymbol{x},t) = M_{pq} * G_{np,q}. \tag{4.12}$$

In a two-dimensional Cartesian system, the explosion source has only the diagonal components of the same magnitude in the moment tensor,

$$\boldsymbol{M} = \begin{pmatrix} M_0 & 0 \\ 0 & M_0 \end{pmatrix}. \tag{4.13}$$

Then the ith component of the displacement can be expressed as

$$u_i(\boldsymbol{x},t) = M_0 * G_{i1,1}(\boldsymbol{x};\boldsymbol{\xi}) + M_0 * G_{i2,2}(\boldsymbol{x};\boldsymbol{\xi}), \tag{4.14}$$

where $\boldsymbol{x}$ and $\boldsymbol{\xi}$ denote the receiver location and the source location, respectively. After applying the spatial reciprocity to equation (4.14), it becomes

$$u_i(\boldsymbol{x},t) = M_0 * G_{1i,1}(\boldsymbol{\xi};\boldsymbol{x}) + M_0 * G_{2i,2}(\boldsymbol{\xi};\boldsymbol{x}). \tag{4.15}$$

$G_{1i}(\boldsymbol{\xi};\boldsymbol{x})$ represents the displacement response in the 1st direction at $\boldsymbol{\xi}$ to the impulse applied in the ith direction at $\boldsymbol{x}$, and $G_{2i}(\boldsymbol{\xi};\boldsymbol{x})$ the response in the 2nd direction at $\boldsymbol{\xi}$ to the same impulse. Hence, the displacement, $u_i(\boldsymbol{x},t)$ at the receiver, $\boldsymbol{x}$, can be calculated by the displacement response at the source, $\boldsymbol{\xi}$, to the single force applied in the ith direction at the receiver, $\boldsymbol{x}$, with the magnitude M_0 as

$$u_i(\boldsymbol{x},t) = \frac{\partial v_1^i(\boldsymbol{\xi},t)}{\partial \xi_1} + \frac{\partial v_2^i(\boldsymbol{\xi},t)}{\partial \xi_2}, \tag{4.16}$$

where

$$v_j^i(\boldsymbol{\xi},t) = G_{ij}(\boldsymbol{\xi};\boldsymbol{x}), \tag{4.17}$$

namely the ith component of the displacement response at the source, $\boldsymbol{\xi}$, to the single force applied in the ith direction at the receiver, $\boldsymbol{x}$, with the magnitude M_0. Since

$$\tau_{ij}(\boldsymbol{\xi};\boldsymbol{x}) = \lambda\delta_{ij}\sum_k \frac{\partial v_k}{\partial \xi_k} + \mu\left(\frac{\partial v_i}{\partial \xi_j} + \frac{\partial v_j}{\partial \xi_i}\right), \tag{4.18}$$

then

$$\tau_{11} + \tau_{22} = (\lambda + 2\mu)\left(\frac{\partial v_1}{\partial \xi_1} + \frac{\partial v_2}{\partial \xi_2}\right). \tag{4.19}$$

Hence equation (4.16) is calculated as

$$u_i(\boldsymbol{x},t) = \frac{\partial v_1^i}{\partial \xi_1} + \frac{\partial v_2^i}{\partial \xi_2} = \frac{\tau_{11}^i(\boldsymbol{\xi},t) + \tau_{22}^i(\boldsymbol{\xi},t)}{\lambda + 2\mu}, \tag{4.20}$$

where $\tau^i(\boldsymbol{\xi},t)$ is a stress component at the location, $\boldsymbol{\xi}$, and time, t, excited by the single force applied in the ith direction at the location, $\boldsymbol{x}$.

Therefore, the displacement, $u_i(\boldsymbol{x}, t)$, at the receiver, $\boldsymbol{x}$, is calculated by the stress components, τ^i_{xx} and τ^i_{zz}, at the location of the source, $\boldsymbol{\xi}$, excited by the single force in the ith direction at the location of the receiver, $\boldsymbol{x}$. The stress field are calculated by the finite difference scheme described in the previous section as equations (4.3) and (4.5). However, equation (4.20) shows that the calculation of the displacement in each direction, i, requires the calculation of the stress field by the single force applied in corresponding direction, in contrast to the forward calculation which requires one wavefield computation excited by an explosive source to obtain displacements in both direction.

4.3 Explosion Source

The source time function of the underwater explosion to be taken convolution of with the synthetic waveforms is modified from that of Spudich & Orcutt (1980). The derivation of the function is based on both theoretical and empirical studies done by Arons, Slifko & Carter (1948), Arons (1948), Arons (1954), and Wielandt (1975). Although they used TNT as explosive sources, its specifications are similar to those of the dynamite used in recent seismic experiments (referred to NG 30) as summarized in Table 4.1. Therefore, the physical parameters of a dynamite source are substituted by those of a TNT source.

Figure 4.3 shows the observed pressure fluctuation in the water which is generated by an explosion of 20 kg dynamite about 30 m deep from the sea surface and recorded about 300 m away from the source epicenter. The observation was recorded with 1 kHz sampling for every explosive shot during the 1994 Nankai experiment. As is seen on Figure 4.3, the source time function consists of three pulses: the first arrival is the

type	Relative Energy (l· kg)	Density	Explosive Velocity (m/s)
NG 93	12.8	1.60	7000
NG 50	7.7	1.53	6800
NG 35	9.8	1.44	6500
NG 30	8.3	1.42	6300
TNT	8.1	1.60	6700

Table 4.1: Comparison of physical parameters among explosive types. The parameters of the dynamite used in the experiment resemble those of the TNT used for the studies by Arons (1948) and others.

shock-wave, and the second and the third arrivals originate from the oscillation of the gas globe. A pressure pulse by the oscillations (which is called bubble, hereafter) is emitted when the bubble oscillation changes the phases from shrinking to expanding. The gas globe migrates upwards with the oscillation of its radius and loses some of the potential energy which is converted to the kinetic energy (Arons et al., 1948). The pulses of the first arrival and the first bubble were unfortunately saturated on the records of all explosive shots (Figure 4.3), and this prevents from discussing the peak amplitudes of those pulses. However, since the pressure fluctuation was sampled at 1 kHz, the arrival times of those pulses were accurately measurable.

The source time function is expressed as

$$P(t) = K\left\{P_0 \exp\left(-\frac{t}{t_0}\right) + P_1 \exp\left(-\left|\frac{t-T_1}{t_1}\right|\right) + P_2 \exp\left(-\left|\frac{t-T_2-T_1}{t_2}\right|\right)\right\}, \quad (4.21)$$

where K is the constant coefficient, P_0 the peak amplitude of the first arrival, P_1 the

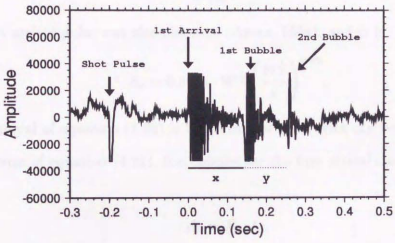

Figure 4.3: Observation of pressure fluctuation excited by an explosive. Phase interpretations are indicated in the figure. x is the time interval between the 1st arrival and the 1st bubble, and y is the time interval between the 1st and the 2nd bubbles.

peak amplitude of the first bubble, P_2 the peak amplitude of the second bubble, T_1 the time interval between the first arrival and the first bubble, T_2 the time interval between the first and the second bubbles, and t_1 and t_2 are the amplitude decay constant for the first and the second bubbles, respectively (Spudich & Orcutt, 1980). Each pulse has a negative exponential dependence on time.

The peak amplitude of the first arrival was determined by an experiment (Arons, 1954), and it is

$$P_0 = 7.60 \cdot 10^3 \left(\frac{W^{\frac{1}{3}}}{r} \right)^{1.13} , \tag{4.22}$$

where W is the charge weight in kilograms and r is the distance from the epicenter in

meters. The impulse, which is defined as

$$A = \int_{t_b}^{t_a} \Delta p \, dt, \tag{4.23}$$

of the first arrival pulse was also observed (Arons, 1954), and it is

$$A_0 = 0.9046 \cdot W^{\frac{1}{3}} \left(\frac{W^{\frac{1}{3}}}{r} \right)^{0.94}. \tag{4.24}$$

As the integral of equation (4.23) is taken from 0 to ∞ with Δp being substituted by the first term of equation (4.21), the impulse for the first arrival can be approximated to be

$$A_0 = P_0 \cdot t_0, \tag{4.25}$$

and t_0 is then calculated from equations (4.22), (4.24) and (4.25). From the theoretical consideration of the total energy associated with the bubble oscillation, E, and of its energy balance, the peak pressure of the first bubble is expressed as

$$P_1 = \frac{P_h L}{r} \frac{\gamma - 1}{k^{\frac{2}{3}(\gamma-1)}} \left\{ 1 - \frac{k^{\frac{1}{\gamma-1}}}{\gamma - 1} \right\}, \tag{4.26}$$

where P_h is the hydrostatic pressure at the depth of explosion, L is the scale factors, $L = \left(\frac{3E}{4\pi P_h} \right)^{\frac{1}{3}}$, and γ is the ratio of heat capacities (Arons, 1948). The parameter k is the function of depth, D, and calculated as $k = 0.074 \cdot Z^{\frac{1}{3}}$ with $Z = D + 10$. After adjusting coefficients to fit P_1 to the observed peak pressure of the first bubble, P_1 is expressed as

$$P_1 = 1.37 \cdot 10^3 \left(\frac{W^{\frac{1}{3}}}{r} \right) \left(1 - k^4 \right). \tag{4.27}$$

The peak pressure of the second bubble is determined so that it fits the observations and it is expressed by taking the proportion to P_1 as

$$P_2 = \frac{P_1}{4.72}. \tag{4.28}$$

According to the theoretical consideration (Arons, 1948), the period of bubble oscillation is expressed as

$$T = C\frac{W^{\frac{1}{3}}}{Z^{\frac{5}{6}}}. \tag{4.29}$$

Figure 4.4 shows the plot of the bubble interval periods observed in the 1994 Nankai-

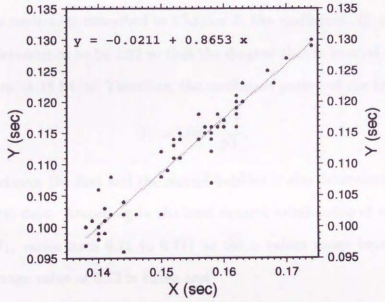

Figure 4.4: Linear relation of bubble oscillation periods. x is the time interval between the 1st arrival and the 1st bubble, and y is the time interval between the 1st and the 2nd bubbles (Figure 4.3).

Trough experiment, where the x axis is taken to be the interval between the first arrival and the first bubble, and the y axis to be the interval between the first and the second

bubbles. The least squares fitting gives the linear relationship of

$$y = 0.8653x - 0.0211. \tag{4.30}$$

As can be seen on the plot, the interval, x, between the first arrival and the first bubble, varies from 0.135 to 0.178. The shortest period, 0.135, corresponds to the deepest shot, whereas the longest period corresponds to the most shallow shot. Since the depth cannot exceed 30 m as the explosive was hung with the 30 m rope from the float at the sea surface as described in Chapter 2, the coefficient, C, in the equation (4.29) is here determined to be 1.08 so that the deepest shot is located at 30.19 m and the most shallow at 18.84 m. Therefore, the oscillation period of the first bubble is

$$T_1 = 1.08 \cdot \frac{W^{\frac{1}{3}}}{Z^{\frac{5}{6}}}. \tag{4.31}$$

The interval between the first and the second bubbles is also determined by observing the experimental data. According to the least squares relationship of equation (4.30), the ratio, T_2/T_1, varies from 0.71 to 0.747 as the x values range between 0.135 and 0.178. The average value of 0.73 is taken and

$$\frac{T_2}{T_1} = 0.73. \tag{4.32}$$

The ratio, T_2/T_1, as well as the theoretical consideration is also used to determine the impulse of the first bubble (Arons, 1948), and the impulse is then written as

$$A_1 = 5.09 \cdot Z^{-\frac{1}{6}} W^{\frac{1}{3}} \left(\frac{W^{\frac{1}{3}}}{r}\right) (1 - 1.6k)^{\frac{1}{2}}. \tag{4.33}$$

The proportion of A_2 to A_1 is obtained from the study of Spudich & Orcutt (1980), and it is

$$A_2 = \frac{A_1}{2.47} \tag{4.34}$$

The decay constants, t_1 and t_2 are calculated by

$$t_1 = \frac{A_1}{2P_1}, \tag{4.35}$$

$$t_2 = \frac{A_2}{2P_2}, \tag{4.36}$$

respectively.

Table (4.2) summarizes the coefficients used in equation (4.21), comparing with those by Spudich & Orcutt (1980).

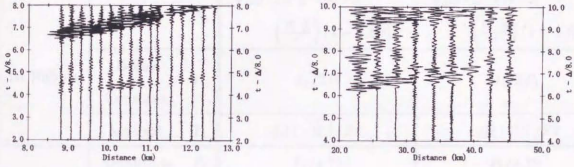

(a) (b)

Figure 4.5: The first arrivals propagating through the crust. (a) Airgun shots. (b) Explosives. No filter is applied.

Figure 4.5.(a) shows the waveforms of the first arrivals of the waves which were generated by the airgun shots and recorded by a digital OBS after they propagated through the crust, and Figure 4.5.(b) shows those generated by the explosive shots. The power spectral densities of the first arrivals are calculated and shown in Figures 4.6.(a) and (b) for airgun shots and explosives, respectively. As can be seen, the waves which propagated through the crust have the dominant frequency around 7 Hz. However, the current computational time for a model with the dimension of 100 km $\times$25 km and for 18 seconds of a waveform whose frequency band is from 0 to 5 Hz is about one day by the parallel computer at Earthquake Research Institute, University of Tokyo. Because

			Spudich & Orcutt	This study
1st Arrival	Amplitude	P_0	$5.25 \cdot 10^5 \left(\frac{W^{\frac{1}{3}}}{r}\right)^{1.13}$	$7.60 \cdot 10^3 \left(\frac{W^{\frac{1}{3}}}{r}\right)^{1.13}$
	Impulse	A_0	$6.69 \cdot 10^3 W^{\frac{1}{3}} \left(\frac{W^{\frac{1}{3}}}{r}\right)^{0.94}$	$0.905 \cdot W^{\frac{1}{3}} \left(\frac{W^{\frac{1}{3}}}{r}\right)^{0.94}$
	Decay Constant	t_0	A_0/P_0	A_0/P_0
1st Bubble	Amplitude	P_1	$1.37 \cdot 10^3 \left(\frac{W^{\frac{1}{3}}}{r}\right)(1-k^4)$	$1.37 \cdot 10^3 \left(\frac{W^{\frac{1}{3}}}{r}\right)(1-k^4)$
	Impulse	A_1	$4.23 \cdot 10^4 Z^{-\frac{1}{6}} W^{\frac{1}{3}} \times \left(\frac{W^{\frac{1}{3}}}{r}\right)(1-1.6k)^{\frac{1}{2}}$	$5.09 \cdot Z^{-\frac{1}{6}} W^{\frac{1}{3}} \times \left(\frac{W^{\frac{1}{3}}}{r}\right)(1-1.6k)^{\frac{1}{2}}$
	Decay Constant	t_1	$A_1/2P_1$	$A_1/2P_1$
	Interval	T_1	$2.11 \cdot W^{\frac{1}{3}}/Z^{\frac{5}{6}}$	$1.08 \cdot W^{\frac{1}{3}}/Z^{\frac{5}{6}}$
2nd Bubble	Amplitude	P_2	$P_1/4.72$	$P_1/4.72$
	Impulse	A_2	$A1/2.47$	$A1/2.47$
	Decay Constant	t_2	$A_2/2P_2$	$A_2/2P_2$
	Interval	T_2	$0.72 \cdot T_1$	$0.73 \cdot T_1$

Table 4.2: Comparison of coefficients in the explosive source time function between those by Spudich & Orcutt (1980) and those obtained in this study.

of this time consumption, the frequency band for the finite difference calculations was chosen to the above range: $0 \sim 5$ Hz.

Figure 4.7.(a) shows the source time function with the parameters obtained by the preceding discussion. The thick solid line on Figure 4.7.(b) shows the low-pass filtered 1st arrival pulse with the frequency band corresponding to the numerical calculations.

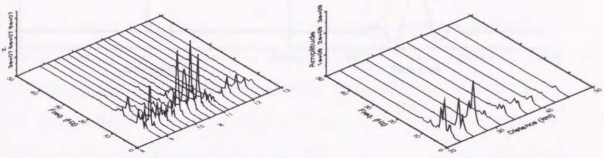

(a) (b)

Figure 4.6: Spectra of the first arrivals propagating through the crust. (a) Airgun shots. (b) Explosives. Waveforms of 1.5 seconds after the arrivals were taken and transformed to their power spectral densities.

Although the decay constants for the three pulses are different (equation (4.21)), their low-pass filtered pulses are not distinguishable from one another, and they are treated as three consecutive pulses of the same shape with different amplitudes. This low-pass filtered pulse cannot be directly input to the numerical calculation, since it generates undesirable numerical dispersion. A smoother function was sought so that the convolution operator for reproducing the actual source pulses is numerically complete. The thin solid line on Figure 4.7.(b) shows the pulse to be input to the numerical calculations. The synthetic waveforms are then calculated with respect to this pulse, and finally the convolution was taken between the results and the present convolution operator to simulate the waveforms generated by the actual source time function. The actual source time function with the frequency band from 0 to 5 Hz is shown on Figure

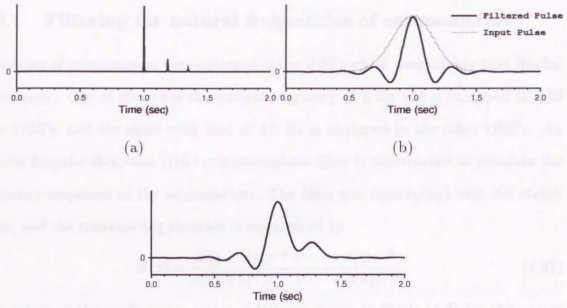

Figure 4.7: Source time function of an explosive. (a) The source time function calculated by equation (4.21). (b) Lowpass-filtered pulse of the first arrival and its substitution for the numerical calculation. Convolution operator to simulate the actual pulse is calculated and operated after the calculation. (c) The actual source time function of the frequency band corresponding to the numerical calculation.

4.7.(c).

4.4 Filtering and Compensation

4.4.1 Filtering for natural frequencies of seismometers

Two types of seismometers were equipped in the OBS's which were used in 1994 Nankai experiment. One of them has the natural frequency of 2 Hz and is equipped in ERI type OBS's, and the other with that of 4.5 Hz is equipped in the other OBS's. An Infinite Impulse Response (IIR) minimum-phase filter is constructed to simulate the frequency responses of the seismometers. The filter was constructed with the eighth order, and the transmitting function is represented by

$$H(z) = \frac{b(0) + b(1)z^{-1} + \cdots + b(8)z^{-8}}{a(0) + a(1)z^{-1} + \cdots + a(8)z^{-8}}. \tag{4.37}$$

The values of the coefficients, $a(i)$ and $b(i)$ are shown in Table (4.3) for the corner frequency of 1 Hz. They are scaled in the use for the actual natural frequencies of the seismometers, i.e., 2 Hz and 4.5 Hz. The calculated synthetic waveforms are filtered to simulate the actual observed waveforms. Figure 4.8 shows the frequency responses of the filter for 2 Hz and 4.5 Hz.

	0	1	2	3	4	5	6	7	8
$a(i)$	1.	-7.7401	26.2854	-51.1531	62.3910	-48.8372	23.9579	-6.7342	0.8304
$b(i)$	0.9823	-7.6381	26.0568	-50.9365	62.4043	-49.0646	24.1759	-6.8254	0.8453

Table 4.3: Coefficients of the filter for compensation of seismometer's natural frequency.

4.4.2 Compensation for attenuation

The synthetic waveform calculations employed in this study do not deal with the inelastic behaviors of the earth present in real observation. Solutions are introduced by

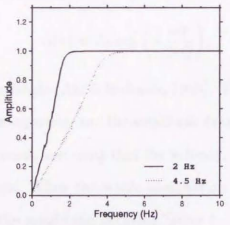

Figure 4.8: Frequency responses of the filters for compensation of seismometers' natural frequencies. Thick solid line is the response for 2 Hz seismometer and thin solid line for 4.5 Hz seismometer.

some authors by incorporating the viscoelastic attitude of the earth's material into the finite-difference calculations (e.g., Robertsson, Blanch & Symes, 1994). It is left over to one of the future subjects to assess and to implement these methods into the calculations. In this study, the attenuation effect is compensated by the following scheme for the part of waveforms near the first arrivals.

The ray paths corresponding to the first arrivals between the sources and the receivers are calculated by the method described in the previous chapter (Fujie, 1996). The quality factors, Q, are assigned to each layer in the model. According to the definition of Q, the derivative of amplitude A with respect to the wave propagation length x is expressed as

$$\frac{dA}{dx} = -\left(\frac{\omega}{2vQ}\right) A, \tag{4.38}$$

where v is the velocity and ω is the angular frequency. And its expression in the integrated form, assuming velocity, v, and Q value are constant, is then

$$A(x) = A_0 \exp\left(-\frac{\omega x}{2vQ}\right), \tag{4.39}$$

where A_0 is the initial amplitude (Aki & Richards, 1980). The ray paths are represented by successive straight line segments, and the amplitude decaying factor, $\exp(-\omega x/2vQ)$, is evaluated for each segment, assuming that the velocity, v, and the Q value are constant through the segment. Then the whole attenuation effect on a ray path is calculated by multiplying the amplitude decaying factor for every segment all together (Figure 4.9).

This scheme evaluates the attenuation effect along the ray paths corresponding to the first arrivals. However, it is possible to claim that the reflected waves which arrives almost at the same time as the first arrivals may follow the similar propagation paths as the first arrivals, and thus may have the similar attenuation effects. The discussion on the waveforms at the proximity of the first arrivals is thus possible, including the attenuation effect of the earth's material.

The Q values assigned to the layers are summarized in Table 4.4.

4.4.3 Compensation for point source

Because the finite-difference calculations in this study are confined to two-dimensional structure with a line source, it is necessary to compensate for this two dimensionality in order to simulate the actual point sources. This compensation is achieved by applying the convolution operator of $1/\sqrt{t}$ to the calculated waveforms. This procedure is explained following Vidale & Helmberger (1987).

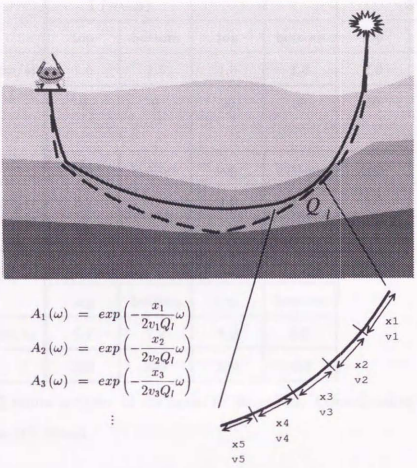

Figure 4.9: Attenuation effect along a ray path of a first arrival calculated by multiplying amplitude decaying factors, $\exp(-\omega x/2vQ)$. The solid line is a ray path of a first arrival and the dashed line is a reflected wave. Propagating paths and travel times of both ray paths are almost the same, indicating both ray paths are affected by the same attenuation effect.

At distance, R, the displacement potential of a spherical wave is

$$\phi_P = \frac{1}{R} f\,(t - R/\alpha)\,, \tag{4.40}$$

layer	1 (water)		2		3	
	top	bottom	top	bottom	top	bottom
Av. Vel. (km/s)	1.5	1.5	1.6	1.8	2.0	2.5
Q	0	0	30	30	60	100
layer	4		5		6	
	top	bottom	top	bottom	top	bottom
Av. Vel. (km/s)	2.8	3.8	4.0	4.4	5.0	5.3
Q	100	100	100	200	250	300
layer	7		8			
	top	bottom	top	bottom		
Av. Vel. (km/s)	6.7	7.2	8.0	8.6		
Q	300	350	350	450		

Table 4.4: Q values assigned to the layers in the model. Corresponding velocities in the layers are also shown.

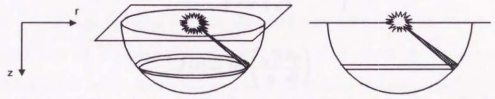

Figure 4.10: Energy spreading for a point and a line sources. The synthetic waveforms calculated for a line source must be transformed to those for an actual point source.

where $f(t - R/\alpha)$ defines a source description, t is time, α is the P-wave velocity (Figure 4.10). The Laplace transformed solution in cylindrical coordinates (Strick,

1959) is

$$\overline{\phi_P}(r,z,s) = f(s)\frac{2s}{\pi}\,\mathrm{Im}\int_0^{i\infty+\delta} K_0(spr)\exp\left(-s\eta\,|z-h|\right)\frac{p}{\eta}dp, \tag{4.41}$$

where s is the transform variable over time, K_0 the modified Bessel function, $\eta = \sqrt{1/\alpha^2 - p^2}$, h is the source depth, z the receiver depth, and δ is a small number that serves to keep the integration path off the complex axis. Using the asymptotic expansion of K_0, which is expressed as

$$K_0(spr) = \sqrt{\frac{\pi}{2spr}}\exp\left(-spr\right)\left(1 - \frac{1}{8spr} + \cdots\right), \tag{4.42}$$

and is valid for large spr, and neglecting other terms than the first term, equation (4.41) becomes

$$\overline{\phi_P}(r,z,s) = \sqrt{\frac{2}{\pi r s}}\,\mathrm{Im}\int_0^{i\infty+\delta}\frac{\sqrt{p}}{\eta}\exp\left\{-s\left(pr + \eta\,|z-h|\right)\right\}dp, \tag{4.43}$$

in which $f(t)$ is assumed to be a step function and hence its Laplace transformed expression is $f(s) = 1/s$. This integral has been solved by the Cagniard-de Hoop method, and with $t = pr + \eta\,|z-h|$, it becomes

$$\phi_P(r,z,t) = \sqrt{\frac{2}{r}}\frac{1}{\pi}\left\{\frac{1}{\sqrt{t}} * J(t)\right\}, \tag{4.44}$$

where

$$J(t) = \mathrm{Im}\left(\frac{\sqrt{p}}{\eta}\frac{dp}{dt}\right). \tag{4.45}$$

On the other hand, the solution for the line source excitation from the work of Gilbert & Knopoff (1961) is

$$\phi_L(r,z,t) = \mathrm{Im}\left(\frac{1}{\eta}\frac{dp}{dt}\right). \tag{4.46}$$

Comparing equations (4.45) and (4.46), it is found that, if $J = \sqrt{p}\,\phi_L$, the point source solution ϕ_P is obtained from the line source solution ϕ_L by the operation,

$$\phi_P = \frac{\sqrt{2}}{r}\frac{1}{\pi}\left\{\frac{H(t)}{\sqrt{t}} * \phi_L\right\}. \tag{4.47}$$

It is assumed that p has a constant value, p_0, so that it is treated as a scale factor, $\sqrt{p_0}$. The approximate seismograms are simulated by the operation described as equation (4.47) to the seismograms excited by the line source. As the result of this approximation, vertically traveling energy, which has smaller value of p, is emphasized.

4.4.4 Compensation for fluctuation of seafloor energy transmission

Amplitude variations among observed waveforms are for the most part the consequences of differences of waves' propagation paths through the earth's structure. However, the variations cannot be explained solely by the path's difference. Figure 4.11.(a) shows the observation by OBS #11 of the consecutive explosive shots whose epicentral distances range from 35 km through 55 km, and Figure 4.11.(b) shows the observation by OBS #12 of the same shots whose epicentral distances then range from 20 km through 40 km. OBS #12 is located about 15 km east to OBS #11. Those figures reveal the amplitude dependence on each explosive shot, i.e., the shots with large amplitude observed by OBS #11 have large amplitude on the observation by OBS #12 and the shots with small amplitude on the record of OBS #11 have small amplitude on that of OBS #12. This implies amplitude variations among the sources themselves rather than the variations caused by the structure. As equation (4.22) shows that the peak amplitude of the explosive source is only a function of the explosive mass, and as the mass is constant for each explosive throughout the experiment, the amplitude dependence on sources can be ascribed to the effectiveness of energy transmission at the seafloor for each source.

Figure 4.12 shows the observation of the single-channel hydrophone streamer towed

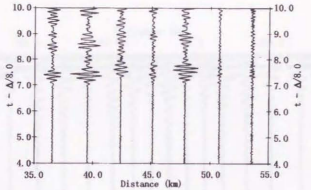

(a)

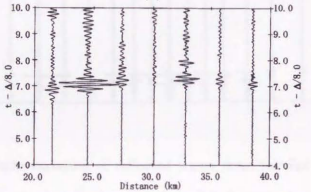

(b)

Figure 4.11: Corresponding amplitude variations over two neighboring OBS's. (a) Waveforms recorded by OBS#11. (b) Waveforms recorded by OBS#12 of the same explosive shots shown in (a). The separation between these two OBS's were 15 km. Although the waves propagated along different paths, the amplitude variations on both records show correspondence. This implies some proportion of amplitude variation is ascribable to explosion-energy fluctuation among shots.

from the tail of the research vessel (Figure 2.2 in Chapter 2). The amplitude variations of the waves reflected at the seafloor are apparent on the record. The compensation for these variations are attained by determining the energy transmission coefficient at the seafloor directly beneath each shot. The coefficient is determined as follows (Figure

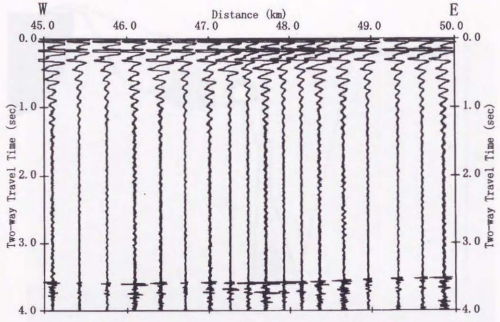

Figure 4.12: Amplitude variation of reflected waves from the flat seafloor. Although amplitude of each airgun shot fired at the time, 0.0, is equivalent to each other, and the seafloor is flat in the region, the amplitudes of reflected waves vary, implying the variation of the reflection coefficient.

4.13). One of the digital OBS is chosen, which is now OBS #12, to determine the transmission coefficient at its location by observing the amplitude ratio of the direct arrival (primary arrival, p_0) and the arrival after reflecting both at the seafloor and at the sea surface (secondary arrival, s_0) of the energy excited by the shot directly above the OBS which is called the reference shot hereafter. The amplitudes of the primary and the secondary arrivals recorded by the OBS are expressed as

$$p_0 = \frac{W}{R_0} \cdot f, \tag{4.48}$$

$$s_0 = \frac{W}{3R_0} \cdot f \cdot (1 - A_0), \tag{4.49}$$

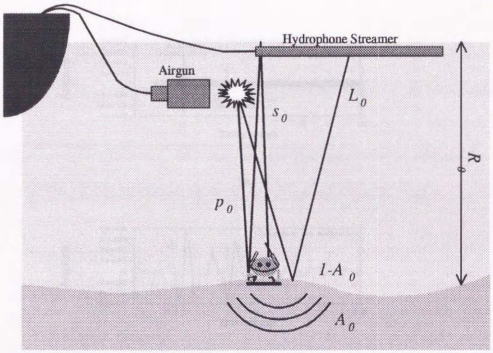

Figure 4.13: Compensation for energy transmission fluctuation at the seafloor. See explanation in text.

where A_0 is the transmission coefficient at the location of the OBS, W represents the magnitude of the reference shot, R_0 is the seafloor depth, f represents the unknown factor acting on the OBS's response to the signal. The ratio of these individual arrivals becomes

$$\frac{p_0}{s_0} = \frac{3}{1 - A_0}. \tag{4.50}$$

Thus the coefficient is calculated by the relation;

$$A_0 = 1 - 3\frac{s_0}{p_0}. \tag{4.51}$$

Figure 4.14.(a) shows the recorded waveform of the reference shot by the OBS #12, and Figure 4.14.(b) compares the primary and the secondary arrivals as the secondary

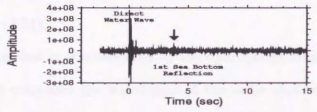

(a)

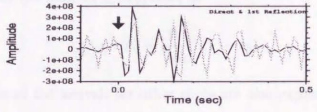

(b)

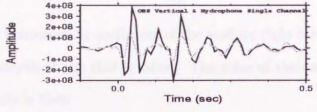

(c)

Figure 4.14: Determination of the transmission coefficients at the OBS location. (a) Waveforms of the first and the reflected arrivals observed by OBS#12. (b) Thick solid line is the first arrival and thin solid line is the reflected arrival. The reflected arrival is multiplied by six so that its amplitude becomes equivalent to that of the first arrival. (c) The first arrival and the waveform observed by SCH. The first half of the SCH data is saturated.

arrival was multiplied by -6 times and they were plotted aligned by the arrival times. As the result, the transmission coefficient at the location is determined to be $A_0 = 0.5$ from equation (4.51).

The reference shot is also observed by the hydrophone streamer at its shot location. Figure 4.14.(c) compares the waveforms of the same shot recorded by the OBS and the hydrophone streamer after adjusting the amplitudes (note that the first half of the arrival recorded by the hydrophone is saturated). The amplitude, L_0, of the arrival reflected once at the seafloor is expressed as

$$L_0 = \frac{W}{2R_0} \cdot (1 - A_0) . \tag{4.52}$$

The amplitudes of the arrivals for other shots are also expressed in the same fashion, and for the ith shot it is expressed as

$$L_i = \frac{W}{2R_i} \cdot (1 - A_i) , \tag{4.53}$$

where A_i is the transmission coefficient of the seafloor right beneath the ith shot, and R_i is the seafloor depth at the shot location. The ratio of the amplitudes of the reference and the ith shots is then

$$\frac{L_0}{L_i} = \frac{1 - A_0}{R_0} / \frac{1 - A_i}{R_i} , \tag{4.54}$$

so that the transmission coefficient, A_i, is determined by the relation,

$$A_i = 1 - \frac{L_i R_i}{L_0 R_0} (1 - A_0) . \tag{4.55}$$

After the transmission coefficient for each explosive shot was obtained, each trace of the OBS records was compensated so that its coefficient was unity.

4.5 Comparisons of the Synthetic Waveforms with the Observed Waveforms

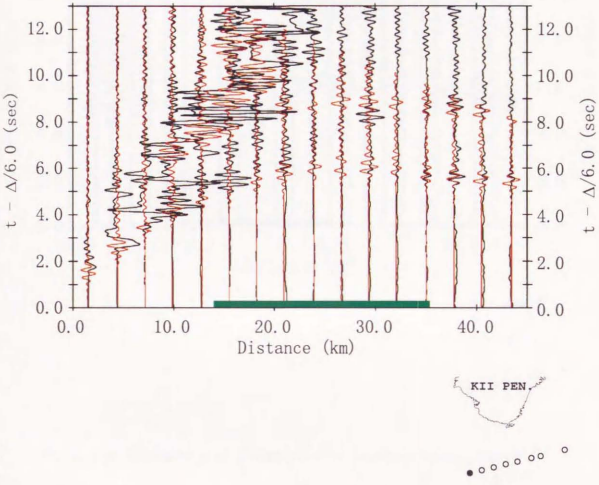

Figure 4.15: Comparison of synthetic and observed waveforms: OBS#10

Figures 4.15 through 4.22 show the comparisons of the synthetic and the observed waveforms of the vertical component. The red traces are the synthetic waveforms and the black are the observed. All plotted traces are compensated for the geometrical

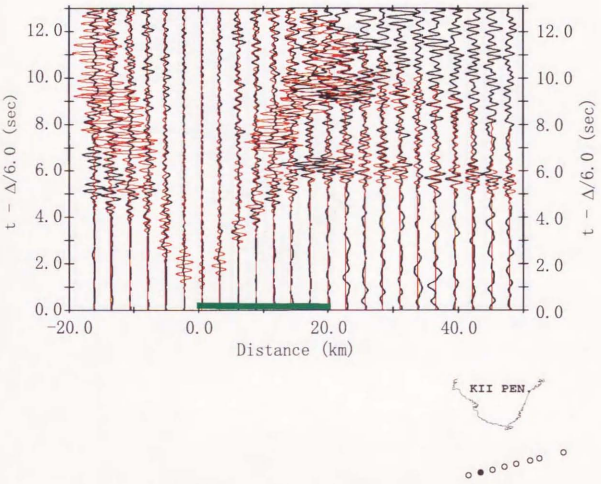

Figure 4.16: Comparison of synthetic and observed waveforms: OBS#11

spreading of energy: the traces are multiplied in proportion to their epicentral distances. The synthetic waveforms were calculated with respect to the model obtained by the travel time inversions discussed in the previous chapter. All the compensations discussed in the previous sections have been applied to the synthetic waveforms. The compensation as to the attenuation accounts for the amplitude of the first arrivals so that precise comparison should be restricted in the proximity of them. However, since

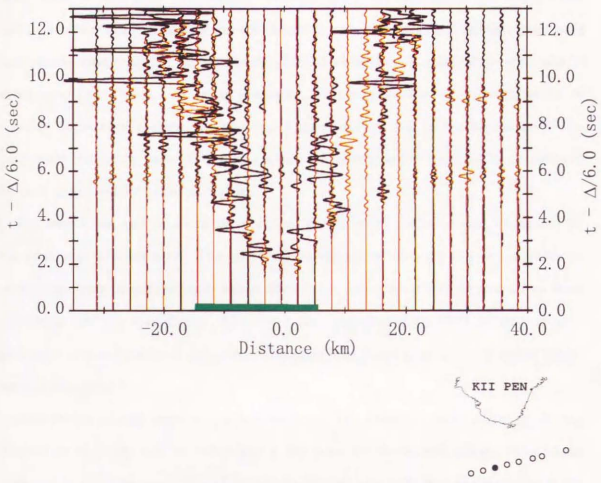

Figure 4.17: Comparison of synthetic and observed waveforms: OBS#12

the frequency band of the calculations is limited from 0 to 5 Hz, the attenuation effect is not very substantial, and it leaves room for comparisons in the other part of waveforms. The discussion on absolute amplitude is not presented here and it is beyond the scope of this paper, since there are still many unknowns in physical properties which are necessary to describe the response of the recording system at the seafloor as a whole. The amplitude of the synthetic waveforms in each plot was multiplied by a factor which

was chosen so that it is comparable to that of the observed waveforms. Fairly good matches between the synthetic and the observed waveforms are seen in both amplitude and phase. However, the amplitude of reflected waves is not sufficiently explained in most cases (see Figure 4.18 for an example). This may be due to underestimation of velocity impedance changes at the velocity interfaces, or due to the limitation of the calculated frequency band ($0 \sim 5$ Hz) whose wave-lengths are too long to be affected by such sharp velocity discontinuities.

The amplitude and phase of the observed direct water waves are not explained by the synthetic seismograms. The observed waveforms of direct water waves suffer in most cases from amplitude saturation when being recorded, which prevented us from discussion on their waveforms. Also the system reaction of an OBS to arrivals with such intense amplitude are unknown. Therefore, the waveforms of direct water waves are not discussed here.

Observation of each comparison is given here. The observed trace whose epicentral location is at x km will be called the x km-trace for short, and always refer to an observed trace. The green line along the horizontal axis indicates the location of the thick sediment, and the blue line indicates the location of the Shionomisaki Canyon.

- OBS #10 (Figure 4.15):

  The large amplitude of the 16 km-trace is of the reflected wave. The amplitudes of the $25 \sim 35$ km-traces are overestimated, and they are large on the synthetic waveforms. Those waves propagated through the anomalously thick sediment, and it can be that physical properties of the sediment are not properly represented by the structure model.

- OBS #11 (Figure 4.16):

Overall good match is observed, except for the reflected waves of the ~ -13 km- and 20 km-traces. The feature that the 33 km-trace has anomalously small amplitude is simulated remarkable well.

- OBS #12 (Figure 4.17):

  Overall good match is observed, except for the 30 km-trace which is overestimated by the reflected wave. Three traces of the observation were absent because of the lack of data. A large amplitude of the 16 km-trace is of the reflected wave.

- OBS #13 (Figure 4.18):

  Overall good match is observed. The two traces of their epicentral distances of about 30 km were of the shots above the Shionomisaki Canyon and their amplitude is small. The effect of rough seafloor topography may not be completely compensated by the transmission coefficients (see Section 4.4) at the seafloor.

- OBS #14 (Figure 4.19):

  Overall good match is observed, except for anomalously large amplitude of the reflected waves of -44 km-trace.

- OBS #15 (Figure 4.20):

  The first arrivals of the $18 \sim 30$ km-traces are filtered out because of their high-frequency-content characteristic. The arrivals with fairly large amplitude within the range are of reflected waves.

- OBS #6 (Figure 4.21):

Overall good match is observed, except for the reflected waves at about 38 km of their epicentral distances.

- OBS #18 (Figure 4.22):

  Overall good match is observed. The western-most two traces with small amplitudes were of the shots above the Shionomisaki Canyon.

4.6 Results

The finite difference synthetic waveform computation method with fourth-order accuracy in space and second-order accuracy in time was modified and developed so that it is easily applied to seismic experiments conducted in the ocean.

Velocity structure to be dealt with in seismic refraction-reflection experiments is often very complex, and the finite difference scheme is most suitable for the model flexibility. The grid is staggered in both space and time, and it works fine for sharp liquid-solid discontinuities. Grid dispersion is also well suppressed.

Reciprocity is incorporated to reduce computational time, since calculation of wavefield for each shot is not realistic. The number of receivers is far less than that of sources. As the difference of the numbers of receivers and sources may differ by an order, reciprocity contributes much for computational time reduction.

Water pressure fluctuation excited by each explosive was recorded by the hydrophone towed behind the vessel. The data were recorded at 1 kHz sampling, and the bubble oscillation period were accurately observed. The source time function of explosive sources was thus precisely determined.

The calculated waveforms are filtered for the natural frequencies of the seismometers

in the OBS's. Two types of seismometers were used during the experiment, with the natural frequencies of 2 Hz and 4.5 Hz. Minimum-phase filters for those two frequencies were constructed and applied in order to simulate the observed waveforms.

Compensation for attenuation effect is applied by considering the attenuation factors along the ray path of the first arrivals. Since the effect is evaluated along the path, the precise discussion on waveforms is restricted to waveforms in proximity of the first arrivals. This will be modified by taking visco-elasticity into account in the waveform calculation.

The finite-difference method employed in this study is limited to two-dimensional calculation. Calibration for a point source is carried out by taking convolution of $1/\sqrt{t}$ with the calculated waveforms.

Amplitude fluctuation of the observed signals is attributable to the crustal structure in most part. However, some portion can be ascribed to energy transmission efficiency of each shot. Amplitude of waves reflected at the seafloor fluctuates although the source energy is constant and the seafloor is flat. Therefore, A part of amplitude fluctuation observed on the obtained data is attributable to the variation of the transmission coefficient at the seafloor, and it is compensated by observing amplitude of reflected waves at the seafloor.

Synthetic seismograms were calculated with respect to the velocity structure model obtained by the travel time inversions discussed in the previous chapter. Good matches are seen between the calculated and the observed refracted waves. These good matches support further the validity of the obtained structural model of the Nankai Trough. However, the waveforms of the reflected waves were not sufficiently explained. It may be caused by the limitation of the frequency band to low frequencies due to the com-

putation time, as the velocity structure is represented by a stack of layers and the velocities change sharply at the interfaces between layers. Waves with long wavelength are expected to be not sensitive enough to such sharp velocity discontinuities. Further studies are necessary to improve fitness of reflected waves.

The good match between the synthetic and the observed waveforms implies the possibility of application of waveform inversions to OBS data. The frequency band was limited to 0 to 5 Hz due to the computational time, and it is desirable to broaden the band toward high frequencies. The computational code used here is left with ample scope of being compacted. This is one of the major subjects of future studies.

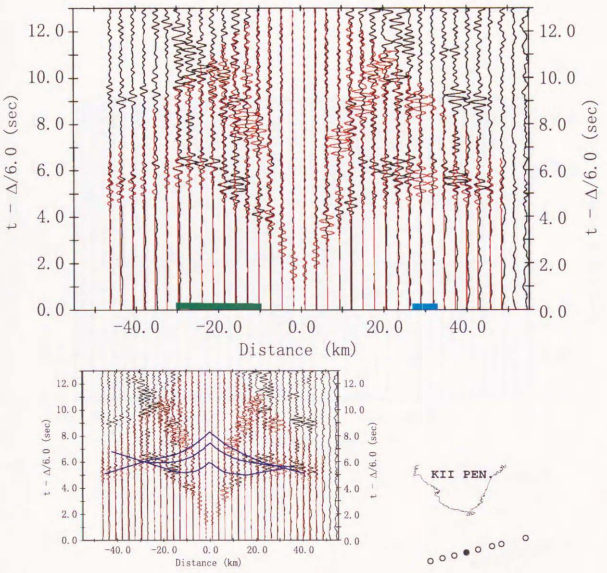

Figure 4.18: Comparison of synthetic and observed waveforms: OBS#13. Blue lines on the bottom figure indicates travel-times of the reflected waves from the three velocity interfaces from the bottom. Amplitude of observed reflected waves are bigger than that of the calculated.

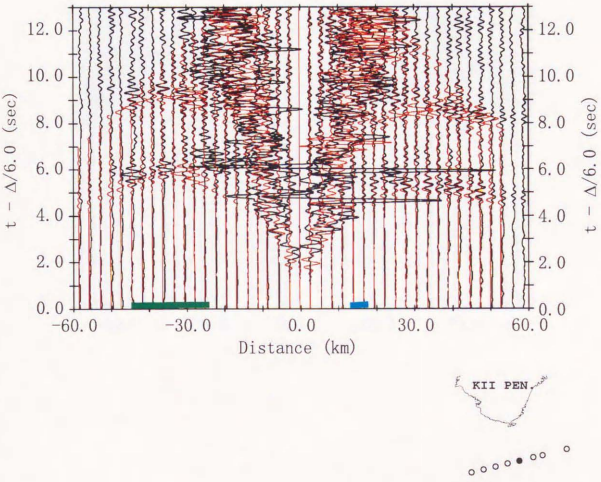

Figure 4.19: Comparison of synthetic and observed waveforms: OBS#14

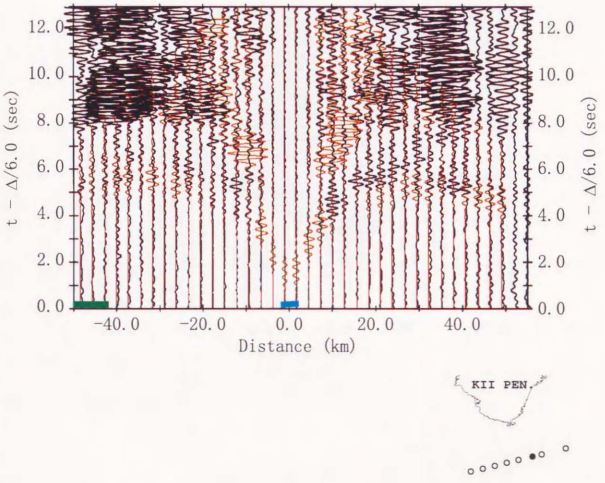

Figure 4.20: Comparison of synthetic and observed waveforms: OBS#15

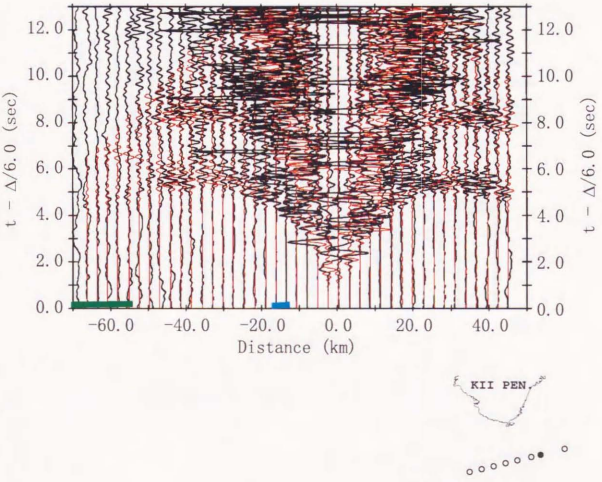

Figure 4.21: Comparison of synthetic and observed waveforms: OBS#6

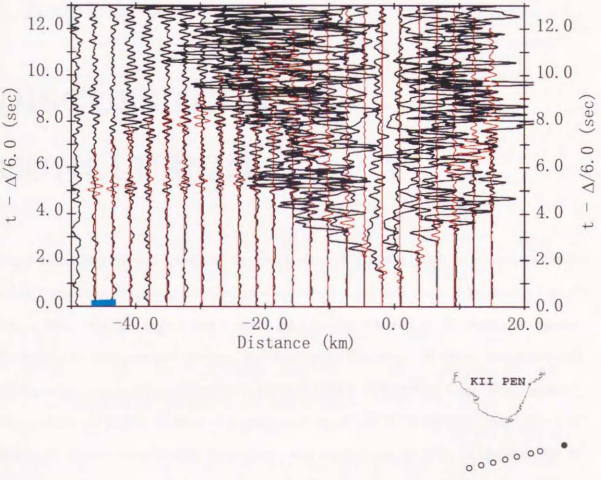

Figure 4.22: Comparison of synthetic and observed waveforms: OBS#18

Chapter 5

DISCUSSION AND CONCLUSION

The Nankai Trough was known as the place where big earthquakes have occurred with a fairly constant recurrence period in a systematic manner: an earthquake occurred first in the Tonankai region and another earthquake followed in the Nankaido region. According to the previous studies, the fault zone boundary of these historical pair earthquakes runs south-eastward from the tip of the Kii Peninsula, Cape Shionomisaki, where there exists the prominent topographic structure of the Shionomisaki Canyon. A seismic refraction-reflection experiment was carried out in 1994 at the location of the expected seismic block boundary, off the Kii Peninsula by the group joined from four organizations.

Airgun shots and explosives were fired along a pair of cross experiment lines: one of them was along the trough axis and the other was perpendicular to it. The objective of the experiment lines were 1) to ascertain whether a positive relationship exists between the structural heterogeneity and the seismic activities (E-W line), and 2) to

obtain precise picture of the Philippine Sea Plate subducting beneath the overriding Eurasia Plate.

The objective of this study was to obtain a precise velocity structure model by applying the newly developed non-linear P-wave travel time inversion technique. The application of non-linear inversions to real data sets has been rarely seen. One of the major reasons is high non-linearity of the inverse problems. The way to suppressing non-linearity was proposed, and finally the non-linear inverse problem was solved for the 1994 Nankai Trough experiment.

The velocity structure obtained by the travel time inversion shows some aspects which draw attention. The crustal thickness of the subducting Philippine Sea Plate changes abruptly beneath the Shionomisaki Canyon, where the seismic boundary is supposed to run. The eastern crust is thicker than the western crust. Figure 5.1 compares the obtained structure model with the previous studies (Murauchi et al., 1964; Murauchi et al., 1968; Yoshii et al., 1973). As is seen on the figure, the crustal thickness of the Philippine Sea Plate becomes thicker in the eastern part. As the result of this study, it is revealed that the thickness changes abruptly, and that its location corresponds to that of the supposed seismic boundary.

The validity of the derived model is confirmed by comparing the synthetic simulation with the real observation about the gravity anomaly and the waveforms.

The theoretically calculated two-dimensional gravity with respect to the derived velocity structure explains the observation remarkably well. The gravity anomaly is positive in the east and negative in the west, which is also simulated by the calculated gravity. The location of the largest change of the gravity coincides with that of the thickness change of the subducting Philippine Sea Plate. The good fit of the gravity

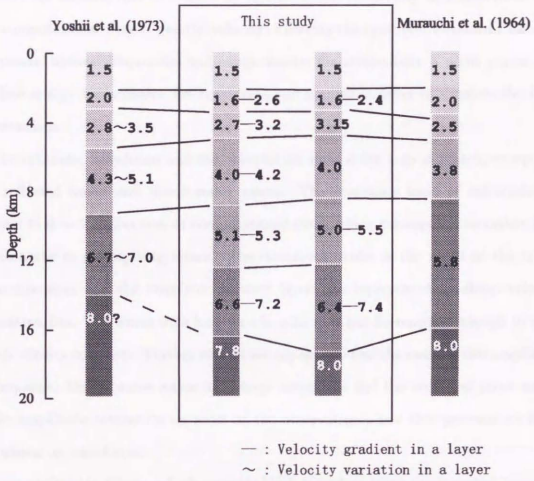

Figure 5.1: Comparison of velocity models along the Nankai Trough. See Figure 1.13 the location of the previous studies by Murauchi et al. (1964),Murauchi et al. (1968) and Yoshii et al. (1973).

data supports the validity of the model.

Synthetic waveforms with respect to this model are calculated by the method developed in this study. The source time function of the explosives is modified from Spudich & Orcutt (1980) based on the precise observation of bubble oscillations. The number

of receivers exceeds that of sources by figures, hence reciprocity is incorporated and the computational time is greatly reduced. Filtering the synthetic waveforms for seismometers' natural frequencies and compensation for attenuation, a point source and seafloor energy transmission are considered and applied in order to simulate the OBS observations.

The synthetic waveforms and the observation show quite a good match, except for the reflected waves and direct water waves. The frequency band of calculation is limited to $0 \sim 5$ Hz because of computational time, which corresponds to rather long wavelengths of propagating waves. The structural model is the result of the travel time inversion, and the interfaces between layers are represented by sharp velocity discontinuities. The waves with long wavelengths may not be sensitive enough to such sharp velocity contrasts. Further studies are required to find the cause of this amplitude discrepancy. Direct water waves have large amplitude and the record of those waves suffer amplitude saturation on most of the observations, and this prevents us from discussion on waveforms.

As is outlined in Chapter 1, the seismic block boundary has been expected to run in the region of the Nankai Trough experiment, off Cape Shionomisaki (Figures 1.3, 1.5, 1.6 and 1.7). And the anomalously concave structure of the subducting Philippine Sea Plate has also been studied, and its steepest fall line coincides with the seismic block boundary (Figure 1.8). The addressed question to the Nankai Trough experiment is whether there is a positive relation between the seismic activity and the crustal structure. The result shows that the crustal thickness of the subducting Philippine Sea Plate changes abruptly beneath the Shionomisaki Canyon and it is interpreted as a structural dividing line runs almost vertically in the upper crust of the subducting

plate. This dividing line is thought to rule the seismic activity of the area. The result also shows that the upper most crust of the subducting plate at the structural boundary has slower P-wave velocity than the surrounding (Figure 3.12).

One interpretation of the mechanism how this structural boundary acts as the rupture zone boundary is given as follows. An earthquake in the Tonankai region occurs and a fault slip propagates toward the Nankaido region, however the slip cannot propagate across the boundary where the crustal thickness changes. The material with slower velocities at the boundary may contribute to stopping the slip propagation as the material has more ductile property and it cannot transmit the slip elastically. The accumulated stress may cause another earthquake in the Nankaido region after some time interval.

The thickness disparity may originate from the complex structure of the Shikoku Basin: Figure 5.2 shows the magnetic anomaly map of the Shikoku Basin and reveals its complex history of evolution. As can be seen on Figure 5.2, the spreading axis runs almost perpendicular to the trough axis, and the age of the crust subducting off the Kii Peninsula becomes older as it goes to the east. The spreading axis changed its trend twice in the history (Figure 1.10), and the crust formed during the latest rotation of the spreading axis is located off the Cape Shionomisaki, where the crust thickness abruptly changes. Therefore, the orientations of the spreading axis were different between the eastern crust and the western crust subducting beneath the Kii Peninsula (Figure 5.2), and its orientation was north-south while the older eastern crust was formed and northwest-southeast while the younger western crust was formed. The spreading axis rotated counterclockwise and the northern crust opened wider during the axis rotation than during the constant opening, which can be easily understood by the fan shape

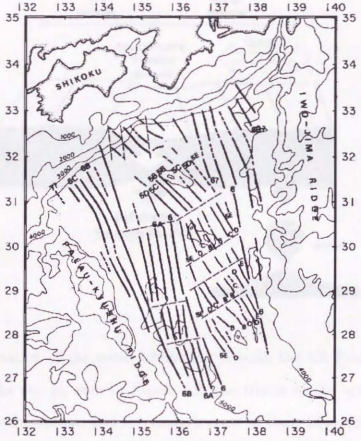

Figure 5.2: Magnetic anomaly map of the Shikoku Basin. The plate off Cape Shionomisaki which is going to subduct beneath the Kii Peninsula was formed during the counterclockwise rotation of the spreading axis.

geometry of the magnetic lineations off the Kii Peninsula (Figure 5.2). If the material supply from the deep along the axis was uniform before and during the axis rotation, the crust formed during the rotation must be thinner compared to the other parts of the crust (Figure 5.3). Or the crust may be stretched more during the rotation, and this may bring about the thinner crust. As the resultant structural model (Figure

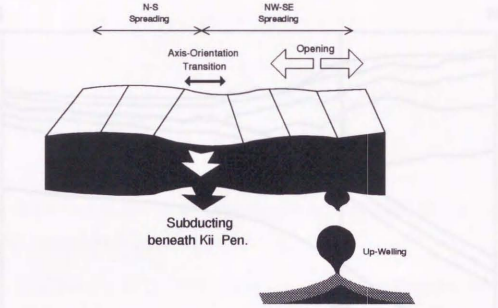

Figure 5.3: Formation of the crust subducting beneath the Kii Peninsula, off Cape Shionomisaki. As can be seen in Figure 5.2, the trends of the spreading axis are different between the eastern and the western crust to Cape Shionomisaki. Rotation of the spreading may result in the variation of the crustal thickness.

3.12) shows the thicker crust of the subducting Philippine Sea Plate in the east to the Shionomisaki Canyon and the thinner crust in the west, the eastern crust must have been formed during the constant opening of the Shikoku Basin, whereas the western crust could be formed during the latest axis rotation.

Finally, the validity of two dimensional analysis is referred to. Figure 5.4 shows the ray path which is originated at 19 km deep beneath the E-W line and is launched vertically upward in the N-S section. The velocity structure along the N-S line is a preliminary result obtained by Nishisaka (Nishisaka, 1997). As is seen in Figure 5.4, the ray propagates strait upward, and this confirms the two dimensional analysis of

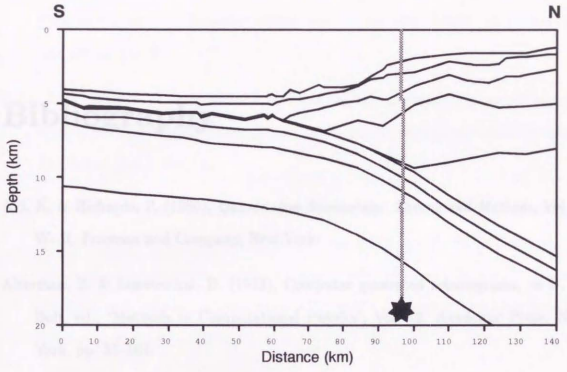

Figure 5.4: Validity of two dimensional analysis. A ray path originated at 19 km deep beneath the E-W experiment line propagating vertically upward is calculated with respect to the velocity structure model along the N-S section. The path propagates strait upward, which confirms the validity of two dimensionality of the analysis along the E-W line.

the velocity structure along the E-W line.

Bibliography

Aki, K. & Richards, P. (1980), *Quantitative Seismology: Theory and Methods*, Vol. 1, W. H. Freeman and Company, New York.

Alterman, Z. & Loewenthal, D. (1972), Computer generated seismograms, *in* B. A. Bolt, ed., 'Methods in Computational Physics', Vol. 12, Academic Press, New York, pp. 35–164.

Ando, M. (1975), 'Source mechanisms and tectonic significance of historical earthquakes along the Nankai Trough, Japan', *Tectonophysics* **27**, 119–140.

Ando, M. (1982), 'A fault model of the 1946 Nankaido earthquake derived from tsunami data', *Phys. Earth Planet. Interiors.* **28**, 320–336.

Arons, A. B. (1948), 'Secondary pressure pulses due to gas globe oscillation in underwater explosions. II. Selection of adiabatic parameters in the theory of oscillation', *J. Acoust. Soc. Am.* **20**(3), 277–282.

Arons, A. B. (1954), 'Underwater explosion shock wave parameters at large distances form the charge', *J. Acoust. Soc. Am.* **26**(3), 343–346.

Arons, A. B., Slifko, J. P. & Carter, A. (1948), 'Secondary pressure pulses due to gas globe oscillation in underwater explosions. I. Experimental data', *J. Acoust. Soc. Am.* **20**(3), 271–276.

Ashi, J. & Taira, A. (1992), 'Structure of the Nankai accretionary prism as revealed from IZANAGI sidescan imagery and multichannel seismic reflection profiling', *The Island Arc* **1**, 104–115.

Ashi, J. & Taira, A. (1993), Thermal structure of the Nankai accretionary prism as inferred from the distribution of gas hydrate BSRs, *in* M. B. Underwood, ed., 'Thermal evolution of the tertiary Shimanto belt, southwest Japan: An example of ridge-trench interaction', Vol. Special Paper 273, Geological Society of America, Boulder, Colorado, pp. 137–149.

Chamot-Rooke, N., Renard, V. & Le Pichon, X. (1987), 'Magnetic anomalies in the Shikoku Basin: a new interpretation', *Earth Planet. Sci. Lett.* **83**, 214–228.

Clayton, R. & Engquist, B. (1977), 'Absorbing boundary conditions for acoustic and elastic wave equations', *Bull. seism. Soc. Am.* **67**, 1529–1540.

Diebold, J. B. & Stoffa, P. L. (1981), 'The traveltime equation, tau-p mapping, and inversion of common midpoint data', *Geophysics* **46**(3), 238–254.

Farnbach, J. S. (1975), 'The complex envelope in seismic signal analysis', *Bull. seism. Soc. Am.* **65**(4), 951–962.

Fitch, T. J. & Scholz, C. H. (1971), 'Mechanism of underthrusting in southwest Japan: A model of convergent plate interactions', *J. Geophys. Res.* **76**(29), 7260–7292.

Fuchs, K. & Müller, G. (1971), 'Computation of synthetic seismograms with the reflectivity method and comparison with observations', *Geophys. J. Roy. Astron. Soc.* **23**, 417–433.

Fujie, G. (1996), New method for travel time and raypath calculations and its application to inversion, Master's thesis, Univ. of Tokyo. in Japanese.

Fukuda, Y. (1990), 'Precise determination of local gravity field using both the satellite altimeter data and the surface gravity data', *Bull. Ocean Res. Inst.* **28**, 1–133.

Gilbert, F. & Knopoff, L. (1961), 'The directivity problem for a buried line source', *Geophysics* **26**(5), 626–634.

Hamilton, E. (1978), 'Sound velocity-density relations in sea-floor sediments and rocks', *J. Acoust. Soc. Am.* **63**(2), 366–377.

Hino, R. (1991), A study on the crustal structure of the Izu-Bonin arc by airgun-OBS seismic profiling, PhD thesis, Tohoku Univ.

Hori, S., Inoue, H., Fukao, Y. & Ukawa, M. (1985), 'Seismic detection of the untransformed 'basaltic' oceanic crust subducting into the mantle', *Geophys. J. Roy. Astron. Soc.* **83**, 169–197.

Ishii, Y., Onishi, M., Aoki, Y. & Muraoka, H. (1995), 'Crosswell tomography for investigating subsurface structure-technical feature and potential', *J. Geography* **104**, 987–997. (in Japanese with English abstract).

Kanamori, H. (1972), 'Tectonic implications of the 1944 Tonankai and the 1946 Nankaido earthquakes', *Phys. Earth Planet. Interiors.* **5**, 129–139.

Kato, S., Sato, T. & Sakurai, M. (1983), 'Multi-channel seismic reflection survey in the Nankai, Suruga and Sagami troughs', *Report of Hydrographic Researches* **18**, 1–23. (in Japanese with English abstract).

Kato, T. (1983), 'High-angle reverse faulting associated with the 1946 Nankaido earthquake', *Tectonophysics* **96**, 31–44.

Kobayashi, K. & Nakada, M. (1978), 'Magnetic anomalies and tectonic evolution of the Shikoku inter-arc basin', *J. Phys. Earth* **26**(Suppl.), 391–402.

Levander, A. R. (1985), 'Use of the telegraphy equation to improve absorbing boundary efficiency for fourth-order acoustic wave finite difference schemes', *Bull. seism. Soc. Am.* **75**(6), 1847–1852.

Levander, A. R. (1988), 'Fourth-order finite-difference P-SV seismograms', *Geophysics* **53**(11), 1425–1436.

Madariaga, R. (1976), 'Dynamics of an expanding circular fault', *Bull. seism. Soc. Am.* **66**(3), 639–666.

Matsu'ura, M. (1991), 'Development of inversion theory in geophysics', *Zisin* **44**(Special Issue), 53–62. in Japanese.

Mizoue, M. (1971), 'Crustal structure from travel times of reflected and refracted seismic waves recorded at Wakayama Micro-earthquake Observatory and its substations', *Bull. Earthq. Res. Inst.* **49**, 33–62.

Mizoue, M., Nakamura, M., Seto, N. & Ishiketa, Y. (1983), 'Three-layered distribution of microearthquakes in relation to focal mechanism variation in the Kii Peninsula, southwestern Honshu, Japan', *Bull. Earthq. Res. Inst.* **58**, 287–310.

Mochizuki, K. (1994), Tomography using a Pseudo-Bending-CG method and its application to the structure of Tsushima basin, Master's thesis, Univ. of Tokyo.

Mochizuki, K., Kasahara, J., Sato, T., Shinohara, M. & Hirata, N. (1997), 'Seismic refraction tomography and its application in an experiment in the Tsushima Basin, Japan Sea', *Butsuri-Tansa -Geophysical Exploration-*. in press.

Murauchi, S., Den, N., Asano, S., Hotta, H., Chujo, J., Asanuma, T., Ichikawa, K. & Noguchi, I. (1964), 'A seismic refraction exploration of Kumano Nada (Kumano Sea), Japan', *Proc. Jap. Acad.* **40**, 111–115.

Murauchi, S., Den, N., Asano, S., Hotta, H., Yoshii, T., Asanuma, T., Hagiwara, K., Ichikawa, K., Sato, T., Ludwig, W. J., Ewing, J. I., Edgar, N. T. & Houtz, R. E. (1968), 'Crustal structure of the Philippine Sea', *J. Geophys. Res.* **73**(10), 3143–3171.

Nishisaka, H. (1997), Crustal structure of the Philippine Sea Plate at subduction and forearc regions along the Nankai Trough off Kii Peninsula, Master's thesis, Chiba University. (in Japanese).

Okamoto, T. (1991), Synthesis of teleseismic P-waves for the study of shallow subduction zone earthquakes, PhD thesis, Univ. of Tokyo.

Okamoto, T. (1994), 'Teleseismic synthetics obtained from 3-D calculations in 2-D media', *Geophys. J. Int.* **118**, 613–622.

Okamoto, T. & Miyatake, T. (1989), 'Effects of near source seafloor topography on long-period teleseismic P waveforms', *Geophys. Res. Lett.* **16**, 1309–1312.

Okino, K. & Kato, Y. (1995), 'Geomorphological study on a clastic accretionary prism: The Nankai Trough', *The Island Arc* **4**, 182–198.

Okino, K., Shimakawa, Y. & Nagaoka, S. (1994), 'Evolution of the Shikoku Basin', *J. Geomag. Geoelectr.* **46**, 463–479.

Robertsson, J. O. A., Blanch, J. O. & Symes, W. W. (1994), 'Viscoelastic finite-difference modeling', *Geophysics* **59**(9), 1444–1456.

Scholz, C. H. (1990), *The Mechanics of Earthquakes and Faulting*, Cambridge University Press.

Seno, T. & Sakurai, T. (1996), 'Can the Okhotsk plate be discriminated from the North American plate?', *J. Geophys. Res.* **101**(B5), 11305–11315.

Seno, T., Stein, S. & Gripp, A. E. (1993), 'A model for the motion of the Philippine Sea Plate consistent with NUVEL-1 and geological data', *J. Geophys. Res.* **98**(B10), 17941–17948.

Spudich, P. & Orcutt, J. (1980), 'Petrology and porosity of an oceanic crustal site: Results from wave form modeling of seismic refraction data', *J. Geophys. Res.* **85**(B3), 1409–1433.

Stephen, R. A. (1983), 'A comparison of finite difference and reflectivity seismograms for marine models', *Geophys. J. Roy. Astron. Soc.* **72**, 39–57.

Stoffa, P. L. (1989), *Tau-p: A plane wave approach to the analysis of seismic data*, Kluwer Academic Publishers.

Stoffa, P. L., Buhl, P., Diebold, J. B. & Wenzel, F. (1981), 'Direct mapping of seismic data to the domain of intercept time and ray parameter - A plane-wave decomposition', *Geophysics* **46**(3), 255–267.

Strick, E. (1959), 'Propagation of elastic wave motion from an impulsive source along a fluid/solid interface. II. Theoretical pressure response', *Philos. Trans. R. Soc. London, Ser. A* **251**, 465–523.

Talwani, M., Worzel, J. L. & Landisman, M. (1959), 'Rapid gravity computations for two-dimensional bodies with application to the Mendocino submarine fracture zone', *J. Geophys. Res.* **64**(1), 49–59.

Červený, V. & Pšenčík, I. (1983), Program package SEIS83, Technical report, Charles University, Prague.

Červený, V., Molotkov, I. A. & Pšenčík, I. (1977), *Ray Method in Seismology*, Univerzita Karlova, Praha.

Vidale, J. E. & Helmberger, D. V. (1987), Path effect in strong motion seismology, *in* 'Computational Techniques', Vol. 4, Academic Press, Inc., Orlando, Florida, chapter 6, pp. 267–319.

Viriuex, J. (1984), 'SH-wave propagation in heterogeneous media: Velocity-stress finite-difference method', *Geophysics* **49**, 1933–1957.

Viriuex, J. (1986), 'P-SV wave propagation in heterogeneous media: Velocity-stress finite difference method', *Geophysics* **51**, 889–901.

Watts, A. B. & Weissel, J. K. (1975), 'Tectonic history of the Shikoku marginal basin', *Earth Planet. Sci. Lett.* **25**, 239–250.

Wielandt, E. (1975), 'Generation of seismic waves by underwater explosions', *Geophys. J. Roy. Astron. Soc.* **40**, 421–439.

Yoshii, T., Ludwig, W. J., Den, N., Murauchi, S., Ewing, M., Hotta, H., Buhl, P., Asanuma, T. & Sakajiri, N. (1973), 'Structure of southwest Japan margin off Shikoku', *J. Geophys. Res.* **78**(14), 2517–2525.

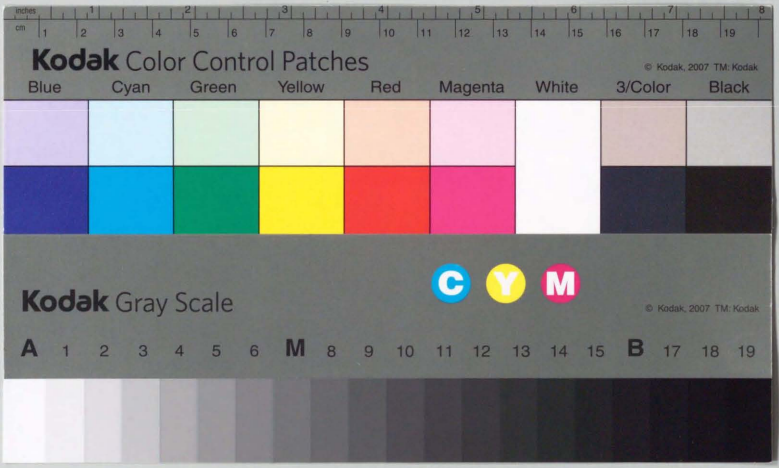
inches
cm
1 2 3 4 5 6 7 8
1 2 3 4 5 6 7 8 9 10 11 12 13 14 15 16 17 18 19
Kodak Color Control Patches
© Kodak, 2007 TM: Kodak
Blue
Cyan
Green
Yellow
Red
Magenta
White
3/Color
Black
Kodak Gray Scale
C
Y
M
© Kodak, 2007 TM: Kodak
A 1 2 3 4 5 6 M 8 9 10 11 12 13 14 15 B 17 18 19